



Review

Two-Dimensional Metal–Organic Frameworks and Their Derivative Electrocatalysts for Water Splitting

Lin Shen ¹, Yongteng Qian ² , Zhiyi Lyu ², Dong-Hwan Kim ¹  and Dae Joon Kang ^{2,*}

¹ School of Chemical Engineering, Sungkyunkwan University, Suwon 16419, Republic of Korea; linshen93@skku.edu (L.S.); dhkim1@skku.edu (D.-H.K.)

² Department of Physics, Sungkyunkwan University, Suwon 16419, Republic of Korea; qytwork@skku.edu (Y.Q.); louislv@skku.edu (Z.L.)

* Correspondence: dj kang@skku.edu

Abstract: The escalating urgency to mitigate climate change and enhance energy security has prompted heightened exploration of hydrogen production via electrocatalysis as a viable alternative to conventional fossil fuels. Among the myriad of electrocatalysts under investigation, two-dimensional (2D) metal–organic frameworks (MOFs) stand out as a particularly appealing option. Their unique properties, including a large active specific surface area, distinctive pore structure, ample metal active sites, ultra-thin thickness, superior ion transport efficiency, fast electron transfer rate, and the ability to control the morphological synthesis, endow these frameworks with exceptional versatility and promising potential for electrocatalytic applications. In this review, we delineate the structural features and advantages of 2D MOFs and their derivatives. We proceed to summarize the latest advancements in the synthesis and utilization of these materials for electrocatalytic hydrogen evolution reactions (HER) and oxygen evolution reactions (OER). Finally, we scrutinize the potential and challenges inherent to 2D MOFs and their derivatives in practical applications, underscoring the imperative for continued research in this captivating field of electrocatalysis.

Keywords: two-dimensional; metal–organic frameworks; derivative; water splitting



Citation: Shen, L.; Qian, Y.; Lyu, Z.; Kim, D.-H.; Kang, D.J.

Two-Dimensional Metal–Organic Frameworks and Their Derivative Electrocatalysts for Water Splitting. *Appl. Sci.* **2023**, *13*, 9343. <https://doi.org/10.3390/app13169343>

Academic Editor: Francis Verpoort

Received: 1 July 2023

Revised: 10 August 2023

Accepted: 15 August 2023

Published: 17 August 2023



Copyright: © 2023 by the authors. Licensee MDPI, Basel, Switzerland. This article is an open access article distributed under the terms and conditions of the Creative Commons Attribution (CC BY) license (<https://creativecommons.org/licenses/by/4.0/>).

1. Introduction

The exacerbating issue of global pollution, coupled with the compelling necessity for an energy paradigm shift, has amplified the demand for renewable energy to decrease our dependence on fossil fuels. Among various alternatives, hydrogen energy [1–3] has been lauded as a potential panacea due to its superior energy density and eco-friendly nature. Electrocatalytic water splitting [4–6], which yields hydrogen from renewable energy sources like wind and sunlight, is an area of intense scientific investigation [7–11]. This process engages two fundamental reactions: hydrogen evolution reactions (HERs) [12–14] and oxygen evolution reactions (OERs) [15–17].

Despite the efficacy of these reactions, their inherent kinetics [18,19] are relatively slow, necessitating catalysts to expedite the processes. Researchers have been meticulously exploring various high-performance catalysts to surmount this obstacle [20–26]. State-of-the-art catalysts such as Pt [27,28] stand out due to their commendable electrical conductivity, high electrocatalytic activity, and near-zero Gibbs free energy, signifying spontaneous reaction. However, the prohibitively high cost and relative scarcity of these noble metals impede their broad-scale application in water electrolysis. Consequently, there is an urgent need to develop highly efficient, non-noble metal electrocatalysts [29–31] that can simultaneously offer high activity and durable longevity for sustained electrocatalysis. Achieving this aim could herald a new era of large-scale hydrogen production from renewable sources, catalyzing the transition towards a more sustainable energy ecosystem.

Introduced in the last two decades, metal–organic frameworks (MOFs) are coordination polymers with intricate three-dimensional (3D) pore structures [32–36]. They are

typically composed of metal ions acting as binding nodes and organic ligands serving as linkers, which collectively form a crystalline, porous network. MOFs exhibit a suite of advantageous properties, including a large specific surface area, low density, high porosity, topological diversity, tunable pore size, regular pore channels, and tailorable functionality [37,38]. Owing to their superior structural controllability and expansive surface area, MOFs are capable of effectively immobilizing enzymes. The tunable pore size and surface properties offered by these frameworks facilitate high efficiency and selectivity in bioseparation and purification processes. Their stable structure, high efficiency in carrier separation and transfer, along with abundant light absorption and catalytic sites render MOFs exceptional photocatalysts. Furthermore, the extensive specific surface area of MOF materials and the interaction between metal ions, ligands, and gases make them particularly suitable for gas adsorption. The versatile MOFs have shown immense potential across a range of applications, including capacitive energy storage [39–41], chemical sensing [42–44], biomedicine [45–47], gas separation [48–50], and storage [51–53]. Yet, the presence of metal nodes enveloped by organic ligands in MOFs often results in poor electrical conductivity, low metal utilization, and hindered ion diffusivity. These drawbacks have fueled research into augmenting the catalytic properties of MOFs and MOF composites through modification of their size, morphology, and composition.

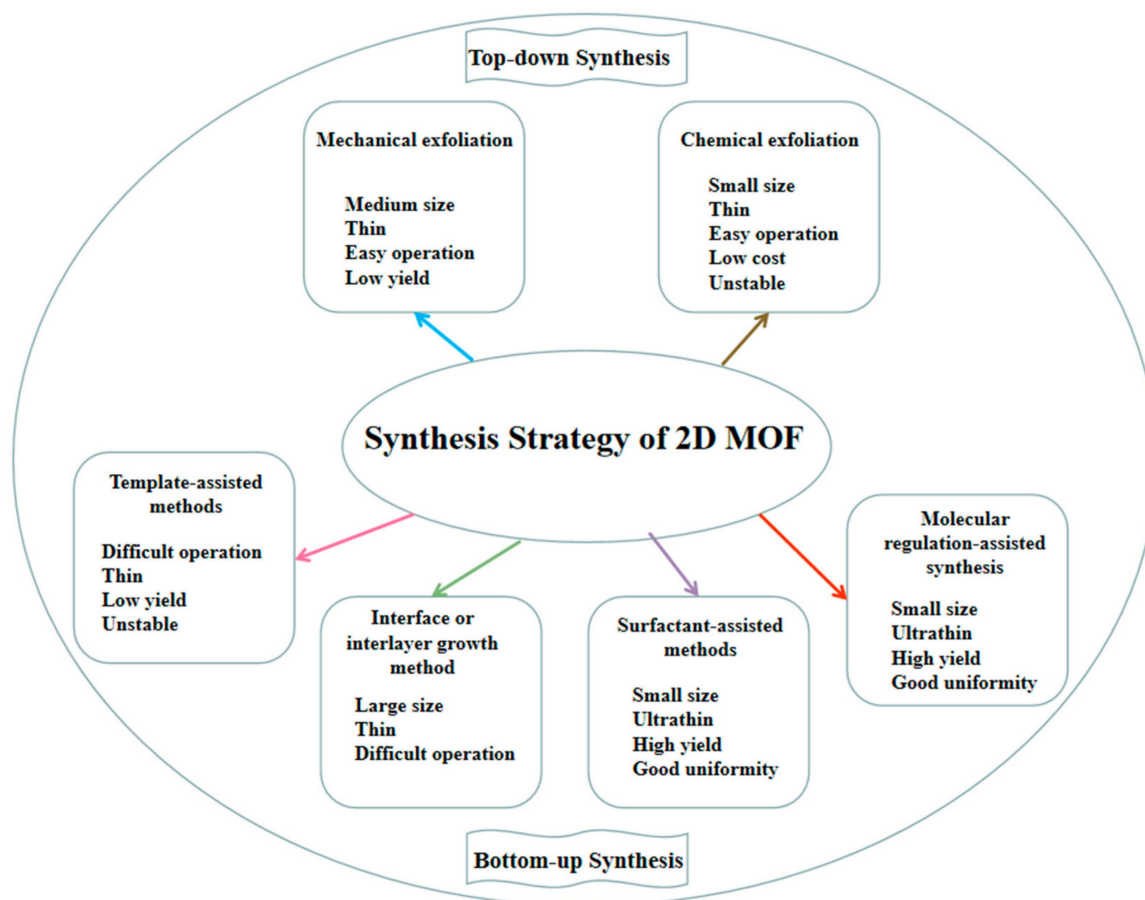
In the wake of the Geim group's groundbreaking isolation of graphene, a single atomic layer of graphite, in 2004, two-dimensional (2D) materials [54–59] have become a focal point of scientific attention. These materials boast extraordinary charge-carrier mobility, efficient thermal diffusion, and unique structural and electronic properties. In contrast to their one-dimensional or 3D counterparts, 2D nanomaterials [60–65] offer expanded specific surface areas and increased exposed interfaces. Furthermore, 2D materials demonstrate superior structural stability compared to zero-dimensional materials, affording them substantial advantages and broad applications in electrocatalysis [66–70]. An emergent subclass of 2D materials, 2D MOFs with a sheet-like morphology [71–76] have displayed enormous potential in the realm of electrocatalysis [77–81]. 2D MOFs incorporate the benefits of 2D materials and MOFs, including larger specific surface areas facilitating more active site exposure, adjustable surface structures via ligand modification, and nanoscale thickness that promotes electron and mass transfer rates. Additionally, 2D MOF derivatives [82–87], which can be transformed into metal/carbon materials through high-temperature carbonization [88] (typically between 700 and 1000 °C), possess excellent electrocatalytic properties owing to their enhanced porosity, optimal exposure of metal sites, and heteroatom doping.

This review aims to provide insight into the recent advancements of 2D MOFs and their derivatives within the realm of electrocatalysis. Initially, we present a comprehensive summary of the preparation strategies adopted for 2D MOFs and their derivatives. Following this, we delve into the detailed exploration of their applications in the sphere of electrocatalytic water splitting. Finally, we discuss the future development prospects of these promising materials in the field of electrocatalysis.

2. Fabrication Strategy of 2D MOF and Their Derivatives

2.1. Fabrication Strategy of 2D MOF

The burgeoning demand for 2D MOFs with diverse properties has stimulated considerable advancements in their fabrication methods over the past years. Typically, the strategies for synthesizing 2D MOF nanosheets can be primarily bifurcated into two distinct paradigms: the top-down and bottom-up approaches (refer to Scheme 1). Top-down fabrication is achieved via the conversion of layered MOFs into nanosheets through chemical or mechanical exfoliation of corresponding bulk materials [89–92]. In contrast, the bottom-up approach entails the direct formation of 2D MOF nanosheets through the strategic assembly of organic linkers and metal ions via ligand interactions [93–97]. This section aims to present an overview of these diverse fabrication methods, underlining their merits and inherent limitations.



Scheme 1. A conceptual representation of the synthesis strategies employed for fabricating 2D MOF materials.

2.1.1. Top-Down Synthesis

Mechanical Exfoliation

The constituent planes of numerous MOF crystals [98,99] are interconnected through weak mutual interactions manifested as hydrogen bonds or van der Waals (vdW) forces. These weak interactions can generally be disrupted by external physical forces [91,92,100–102], thus separating the layers from one another.

In a seminal study conducted by Zamora and team in 2010 [103], a 2D hybrid valence copper ligand polymer $[\text{Cu}_2\text{Br}(\text{IN})_2]_n$ (IN = isonicotinato) was subjected to ultrasonic treatment, leading to the generation of 2D MOF nanosheets. The underlying geometric configuration of this compound constitutes a four-ligand unit, in which the ligands along the bc plane direction bridge the $[\text{Cu}_2\text{Br}(\text{IN})]_4$ units into a 2D wavy structure. The bromine ligands reside on both sides of this plane, resembling the structure of the iodine complex. Given the structural similarities of $[\text{Cu}_2\text{Br}(\text{IN})_2]_n$ with graphite, the team employed ultrasound as a physical means to attenuate the interlayer forces in the coordination polymer, analogous to the method used to extract graphene from graphite. As a result, the 2D nanosheets, exhibiting a uniform height of $5 \pm 0.15 \text{ \AA}$, were successfully distributed in layered formation on substrates of highly oriented pyrolytic graphite, as revealed by atomic force microscopy (AFM).

Apart from the ultrasonic exfoliation technique, micromechanical exfoliation methods also exist. These methods generally utilize physical forces applied by grinding [104] or sphere milling [105] to disrupt the interlayer forces in the bulk material, subsequently separating the layers to yield nanosheets. In one instance, Ma et al. [106] employed a combination of wet sphere milling and ultrasonication to exfoliate ZSB-1 ($\text{Zn}_2(\text{SBA})_2(\text{BPTP})$), SBA = 4,4'-sulfonylbiphenzoic acid, BPTP = 3,5-bis(5-(pyridin-4-yl) thiophen-2-yl)pyridine)

into ultra-thin, rectangular nanosheets. Figure 1a illustrates the process of synthesizing 2D ZSB-1 nanosheets. The thickness distribution of the 2D sheet was assessed using AFM images, with a flat, smooth platform of 11.8 ± 2.3 nm observed for the ZSB-1 nanosheet in the height profile (Figure 1b). Transmission electron microscopy (TEM) and scanning electron microscopy (SEM) images (Figure 1c,d) indicated that the structural integrity of the ZSB-1 nanosheets was maintained following wet ball milling and ultrasonic treatment. These images clearly depicted the undamaged rectangular structure of the ZSB-1 nanosheets, confirming the successful preservation of their morphology. Importantly, the crystalline structure of the nanosheets remained intact after treatment, underlining the high stability of the material.

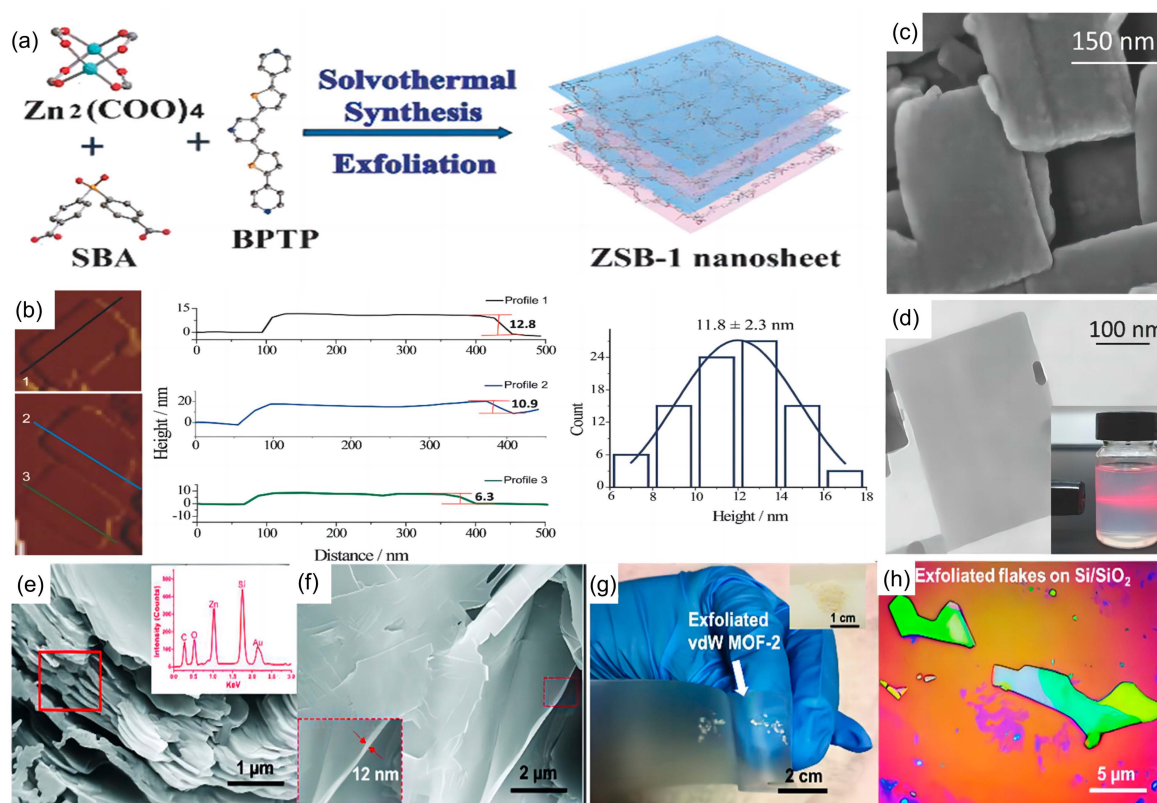


Figure 1. (a) The fabrication process of ZSB-1 nanosheets. (b) AFM analysis of exfoliated ZSB-1 nanosheet and corresponding height contours. (c) SEM image of an exfoliated ZSB-1 nanosheet. (d) TEM image of an exfoliated ZSB-1 nanosheet. Reproduced with permission [106]. Copyright 2018, Wiley-VCH. (e) SEM image of vdW MOF-2 sheets exhibiting a thickness of 10 nm and lower. (f) SEM image of large lateral single-crystal sizes. (g) Tape exfoliation process. (h) Exfoliated flakes on Si/SiO₂. Reproduced with permission [107]. Copyright 2018, Wiley-VCH.

In another example, Tongay et al. [107] employed transparent adhesive strips to mechanically peel-off vdW MOF-2, a method known as micro-mechanical exfoliation. Figure 1e shows the characteristic lamellar architecture of the deposited MOF-2 crystals, with SEM images illustrating the sheet-like slices (≈ 10 nm) of vdW crystals (Figure 1e,f). The monolayers in these crystals were separated using transparent tape and subsequently deposited on a substrate (Figure 1g,h). Sphere milling serves as another viable approach to induce physical forces, demonstrated by the suspension of Zn₂(bim)₃ (bim = benzimidazole) nano-flakes via sphere milling. Despite the relative simplicity of mechanical exfoliation, it suffers from certain limitations, such as issues with reproducibility and challenges in obtaining uniform nanosheets. For instance, Yang et al. [108] combined wet sphere milling with ultrasonic treatment to exfoliate 2D Zn₂(bim)₃ MOFs, resulting in Zn₂(bim)₃ nanosheets with a thickness of 1.6 nm. Despite this success, the physical synthesis method

has notable drawbacks, such as low yield and unstable storage. Therefore, the development of more efficient methods to overcome these challenges is a significant area of interest.

Chemical Exfoliation

To circumvent the challenges posed by mechanical or solvent-mediated exfoliation processes, controlled chemical reactions can effectively manipulate interactions between layers to generate synthetic ultrathin 2D nanosheets [89,90]. In a pioneering study conducted by Zhou et al. [109], the researchers achieved chemical exfoliation of intercalated MOF crystals to produce high-yield 2D MOF nanosheets. This was performed by incorporating the chemically unstable 4,4'-dipyridyl disulfide (DPDS) ligand into the layered MOF crystal to create a novel inserted MOF, followed by the reduction of disulfide bonds with trimethylphosphine (TMP) (Figure 2a). By weakening the interactions between the DPDS-swollen 2D layers, the researchers were able to easily exfoliate the MOF into ultra-thin (~1 nm) nanosheets with an impressive product yield (~57%).

Zheng et al. [110] demonstrated an alternative approach by altering the pH and chemically exfoliating the MOF into negatively charged nanosheets. This was achieved by introducing protonated phosphonate groups into the layers of $[\text{Co}(\text{Ni-H}_7\text{TPPP})_2] \cdot 8\text{H}_2\text{O}$ (TPPP = 5,10,15,20-tetrakis[*p*-phenylphosphonic acid]porphyrin). In a quest for a more effective way to break the coordination bonds between MOF crystal planes, Zhang et al. [111] utilized chemical oxidation in an electrochemical exfoliation method. In this method, catechol-functionalized pillars were oxidized and removed during the electrochemical process, resulting in ultra-thin nanosheets (2 nm) (Figure 2b). Despite being cost-effective and easy to handle, top-down synthesis of 2D MOF nanosheets has limitations such as precursor requirements, low yield, and challenges with stacking synthesized products, which restricts its applicability on a large scale.

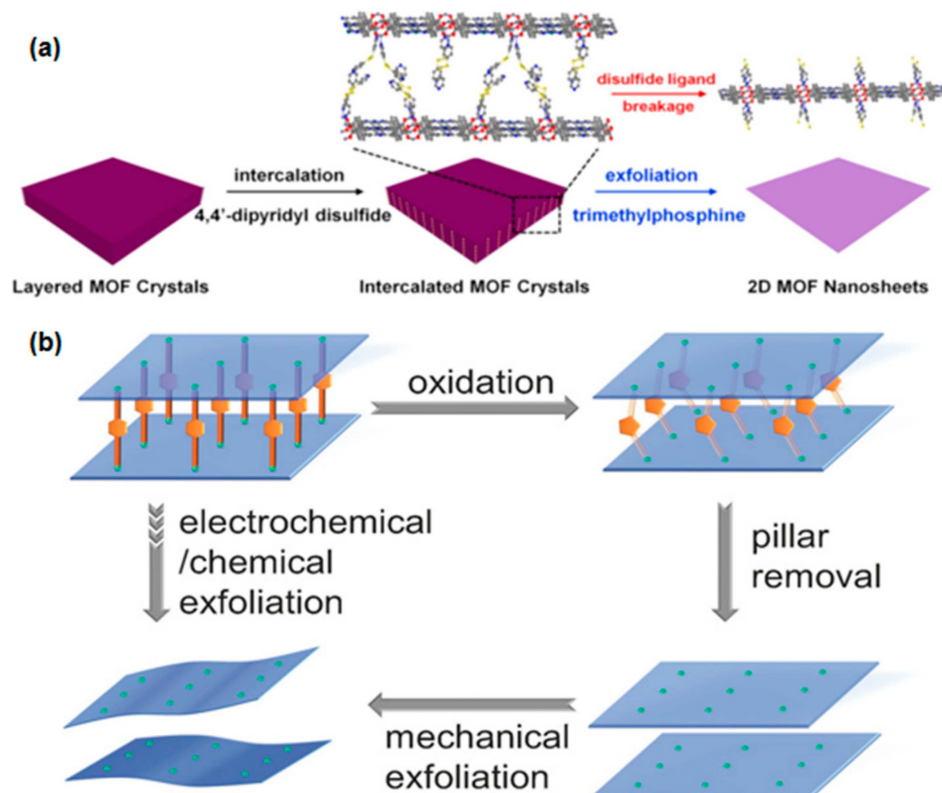


Figure 2. (a) Depiction of the intercalation and chemical exfoliation method for the synthesis of 2D MOF nanosheets. Reproduced with permission [109]. Copyright 2017, American Chemical Society. (b) Process of interlayer pillar removal for the synthesis of 2D MOF. Reproduced with permission [111]. Copyright 2018, Wiley-VCH.

2.1.2. Bottom-Up Fabrication Formwork-Assisted Methods

Formwork-assisted methods encompass hard formwork and sacrificial formwork strategies. The hard formwork technique facilitates the controlled deposition of a desired substance onto a substrate, thereby dictating the growth pattern of the 2D MOFs based on the substrate type. Li et al. [112] exemplify this approach by coating a polyacrylonitrile (PAN) substrate with poly(sodium-p-styrenesulfonate)-modified (PSS) halloysite nanotubes (HNTs), followed by the deposition of zeolitic imidazolate framework-L (ZIF-L) onto the support surface (Figure 3a). The consistent arrangement of HNTs crucially impacts the growth direction of ZIF-L, especially for substrates with uniform PSS-functionalized HNT loading, where the initial ZIF-L crystallization tends to occur horizontally on the surface (Figure 3b,c).

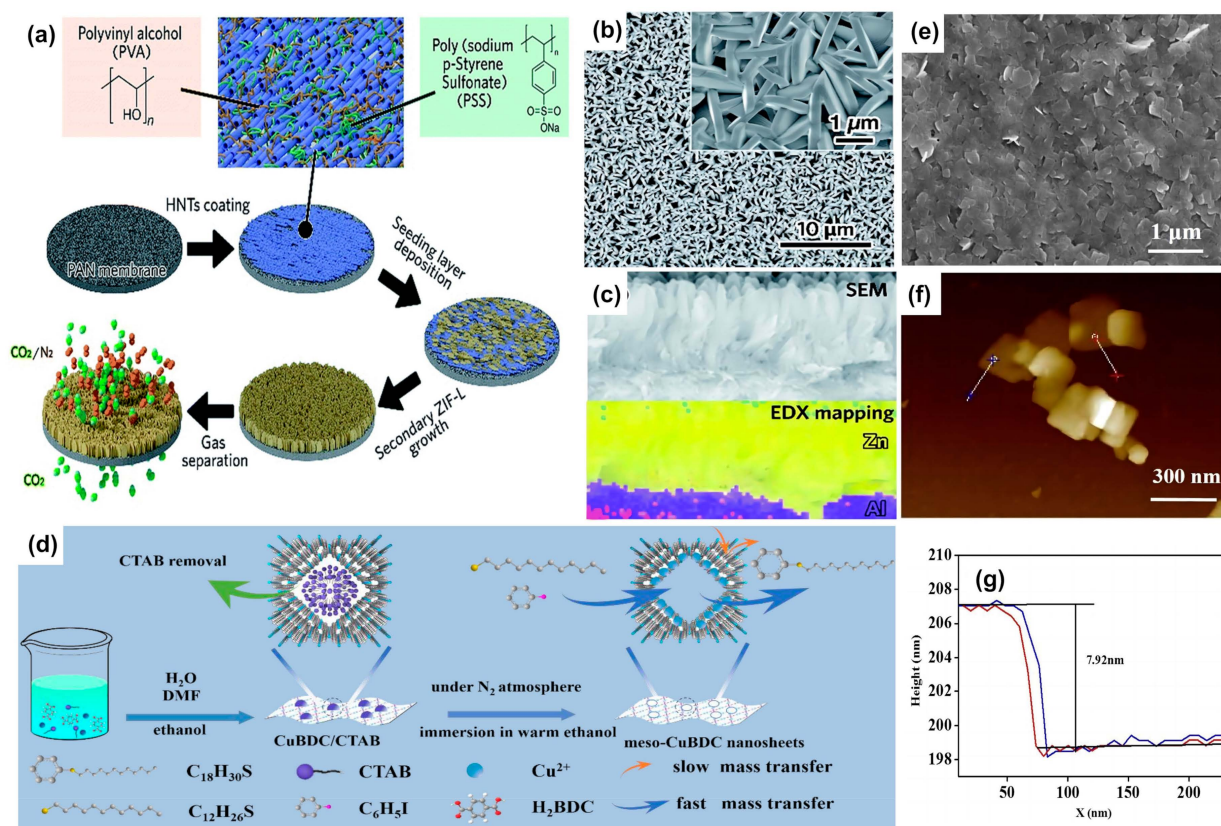


Figure 3. (a) Schematic representation of the PAN-HNTs-ZIF-L film preparation process. (b) SEM image showcasing the top-surface morphology of the PAN-HNTs-ZIF-L film. (c) SEM image complemented by Energy Dispersive Spectrometry mapping, providing elemental analysis of the cross-sectional region of the PAN-HNTs-ZIF-L film. Adapted with permission from [112]. Copyright 2019, Royal Society of Chemistry. (d) A step-by-step diagram of the synthesis procedures resulting in meso-CuBDC nanosheets. (e,f) Detailed SEM and AFM images revealing the structural properties of meso-CuBDC nanosheets. (g) Histogram illustrating the thickness distribution of the meso-CuBDC nanosheets. Adapted with permission from [113]. Copyright 2020, Elsevier.

On the other hand, Wei et al. [113] utilized the surfactant cetrimonium bromide (CTAB) as a sacrificial template to synthesize mesoporous MOF nanosheets. Upon adding a Cu(CH₃COO)₂ solution to a mixed solution of CTAB and 1,4-dicarboxybenzene (H₂BDC) at room temperature, and subsequent removal of CTAB with hot ethanol, meso-CuBDC MOF nanosheets were obtained (Figure 3d). The SEM image (Figure 3e) displays the nanosheet morphology of the CuBDC, with its mesoscopic structure displaying uniform dispersion within 200~300 nm and a small square shape. The mesoscopic CuBDC nanosheets were

meticulously characterized using AFM. These nanosheets are approximately 200 nm in size, possess a square shape (as depicted in Figure 3f), and maintain a thickness of less than 8 nm (refer to Figure 3g), thus underscoring the precision in our preparation method.

In parallel, Han et al. [114] achieved the synthesis of ultrathin NiCo-layered double hydroxide@MOFs nanosheets (NiCo-LDH@MOFs) utilizing an in situ semi-sacrificial formwork-assisted approach. This procedure initiated the synthesis of NiCo-LDH nanosheets as precursors through a hydrothermal method. These nanosheets were subsequently deprotonated with H₂BDC, allowing the metal within the NiCo-LDH to coordinate and form bimetal MOFs (BMOFs) nanocrystals in situ. The nanocrystals thus formed on the LDHs' surface and then served as secondary growth nucleation sites for BMOFs. Ultimately, the ultra-thin BMOF nanosheets were obtained through secondary growth on the NiCo-LDHs surface.

While the formwork-assisted synthesis method can engineer 2D MOFs with controlled morphology, it presents some drawbacks. Firstly, the synthesis procedure is rather intricate, which can limit its broader application. Additionally, the method yields a modest quantity of product. Thus, it is paramount for researchers to refine the synthesis method and route to augment the yield at each step of the formwork-assisted synthesis, thereby improving overall efficiency and scalability.

Interface or Interlayer Growth Method

Two-phase interface synthesis processes generally encompass methods involving liquid–gas, liquid–liquid, solid–liquid, and solid–gas interfaces. In these, organic linkers and metal ions are initially distributed in two phases, then diffused to the two-phase interface, and finally reacted at the interface to yield 2D MOF nanosheets. Solid–gas interface synthesis encounters limitations due to challenging synthesis conditions and methods. However, the liquid–gas, solid–liquid, and liquid–liquid interface methods have gained significant attention due to their milder synthesis conditions.

Chen et al. [115] demonstrated the synthesis of highly conductive 2D MOF films through a liquid–liquid interface reaction, combining the organic ligand benzhexanethiol (BHT) with Au or Ag ions (Figure 4a). The Ag₃BHT₂ MOF film produced showed excellent conductivity of up to 363 S cm⁻¹. X-ray diffraction analysis revealed a hexagonal lattice structure in Ag₃BHT₂, which enables planar conjugation and π - π superposition, contributing to its high conductivity. In contrast, Au₃BHT₂, with its disordered structure, exhibited nearly insulating properties (Figure 4b,c). The Ag₃BHT₂ 2D MOF thin film offers promising applications in electronic devices and sensors due to its excellent conductivity and straightforward synthesis method.

In 2021, Wang et al. [116] reported the synthesis of 2D Ni-MOF nanosheets through a liquid–liquid interface reaction. By controlling the molar ratio of organic linkers and metal ions in different solvents, they precisely controlled the coordination mode of Ni-MOF nanosheets. This led to highly efficient 2D MOF nanosheets with near-zero overpotential and approximately 98% selectivity for H₂O₂ when the metal ion/organic ligand concentration was 6. The average thickness of Ni-MOF nanosheets was approximately 5 nm (Figure 4d). Although the liquid–liquid interface synthesis presents an advantage of simple synthesis and controllable product components or morphology, the limited contact interface area between the two-phase solutions restricts its synthesis efficiency.

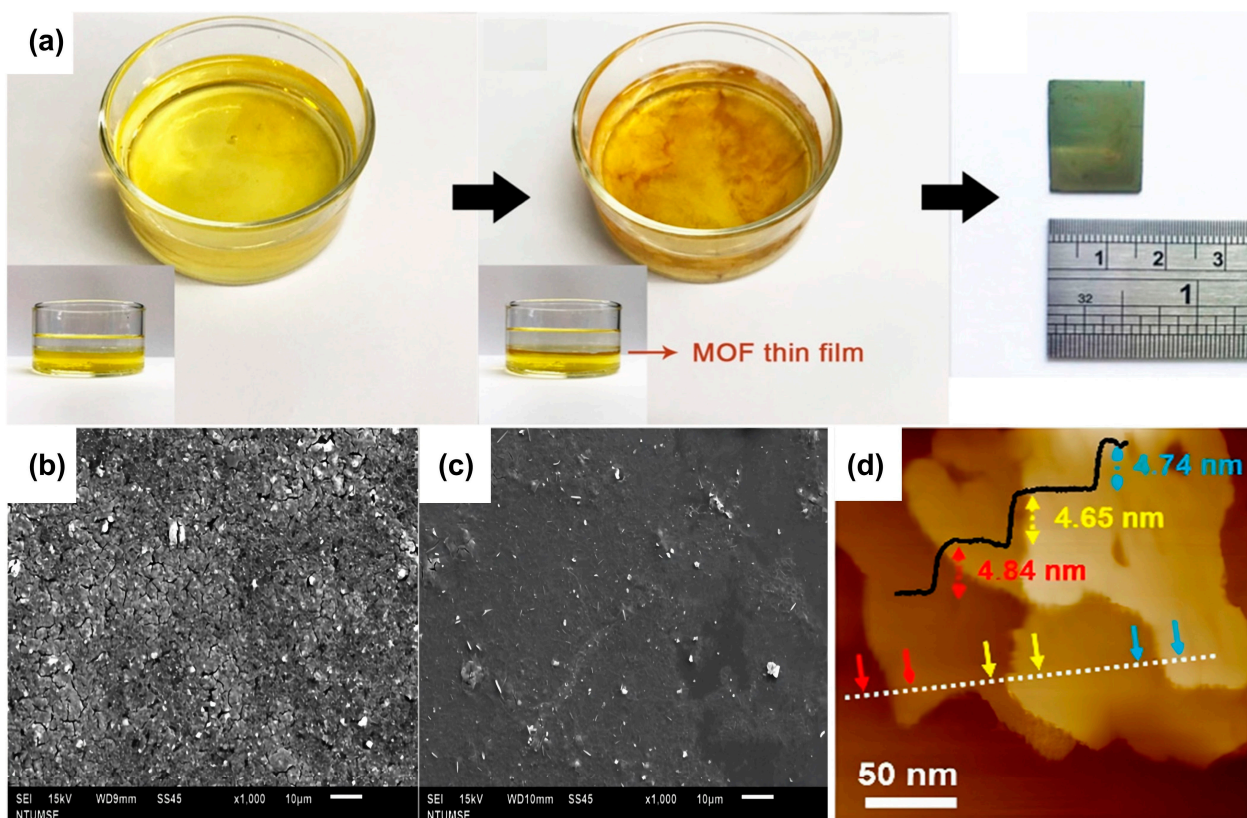


Figure 4. (a) Ag_3BHT_2 thin slice formed via liquid–liquid interfacial approach. (b) Thin slice Ag_3BHT_2 SEM image. (c) Thin slice Au_3BHT_2 SEM image. Reproduced with permission [115] Copyright 2018, American Chemical Society. (d) Ni-MOF nanosheets-6 AFM image and the corresponding height profiles. Reproduced with permission [116]. Copyright 2021, Wiley-VCH.

Tania Rodenas et al. [117] proposed an interfacial synthesis method involving three solvent layers and two pure solvents:—acetonitrile and dimethylformamide (DMF), which are miscible—and a mixed layer of DMF and acetonitrile. BDC ligands in the bottom layer and copper ions in the top layer gradually diffuse into the middle DMF and acetonitrile mixed layer, forming 2D nanosheets with a thickness of approximately 5–25 nm and lateral dimensions of 0.5–4 μm . This method mitigates the limited interfacial contact area issue of liquid–liquid interfacial synthesis, but the limited space still presents a constraint, making it less favorable for large-scale applications.

Surface-Active Agent-Assisted Methods

Surface-active agent-assisted synthesis methods have proven effective in directing the growth of MOF crystals. In this method, surfactants bind to the surface of MOF crystals, inhibiting their vertical growth and enhancing growth in the 2D direction.

For instance, Zhang et al. [118] successfully prepared ultra-thin 2D Zn-TCPP (TCPP = tetrakis(4-carboxyphenyl)porphyrin) nanosheets with a thickness of less than 10 nm using a surface-active agent-assisted method. They used polyvinylpyrrolidone (PVP) as a surfactant to limit the expansion of MOF crystals in-plane by adhering to the MOF surface during the synthesis of Zn-TCPP. This resulted in different growth rates of the MOF in different directions. The C=O group in the PVP surfactant strongly interacts with the metal ions in MOF, facilitating PVP's attachment to the MOF's outer layer post-nucleation and restraining its expansion. The scanning transmission electron microscopy (STEM) images show Zn-TCPP nanosheets with an area of approximately $1.2 \pm 0.4 \mu\text{m}^2$, while the high-resolution TEM (HRTEM) image reveals an interplanar distance of 1.64 nm for Zn-TCPP nanosheets.

Zheng et al. [119] fabricated bimetallic 2D Co/Zn-porphyrin MOF nanomaterials using a surfactant-assisted method (Figure 5a). SEM and TEM images (Figure 5b,c) depict that Co/Zn-porphyrin displayed wrinkled nanofilm structures. Introducing PVP to Co/Zn with different molar ratios limited the vertical expansion of MOFs and promoted the 2D growth of MOFs, resulting in bimetallic 2D MOF nanomaterials with thicknesses of 4–5 nm (Figure 5d).

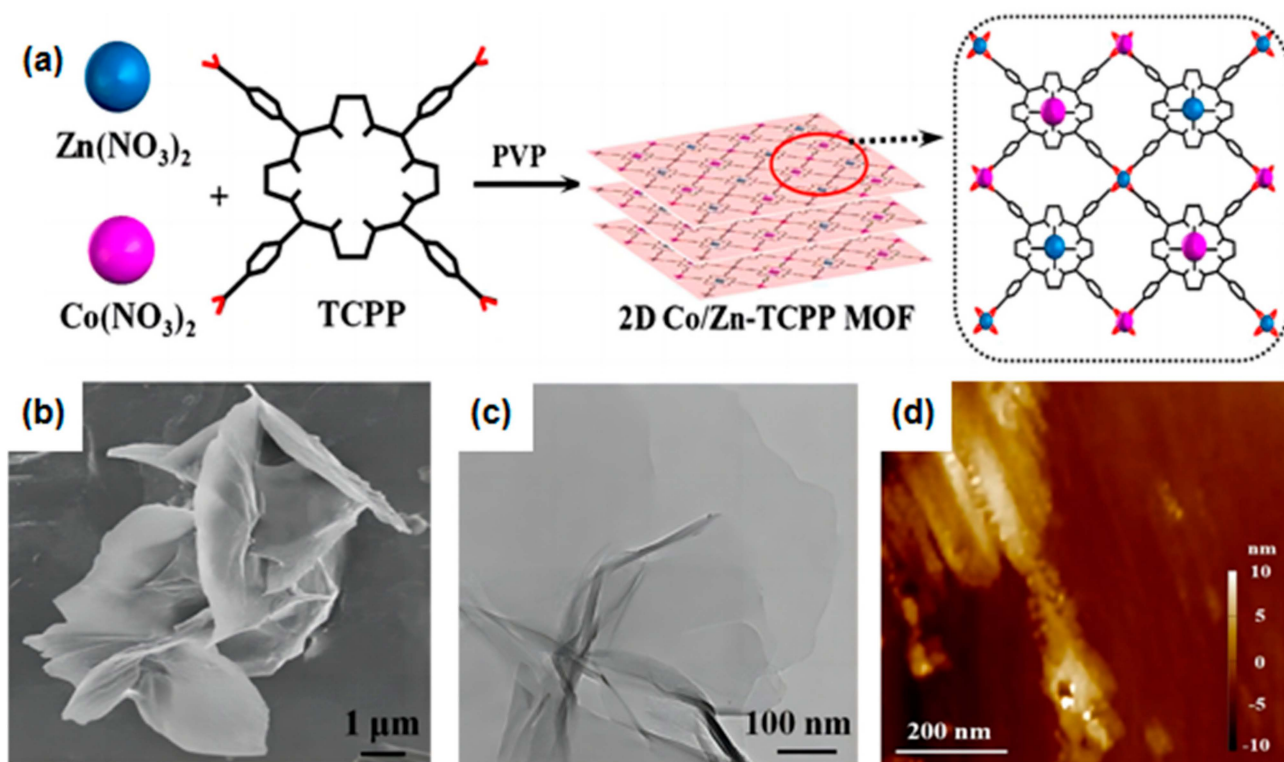


Figure 5. (a) Synthetic process of 2D Co/Zn-porphyrin MOF nanosheets. (b) Co/Zn-porphyrin SEM image. (c) Co/Zn-porphyrin TEM image. (d) Co/Zn-porphyrin AFM image. Reproduced with permission [119]. Copyright 2021, Springer Nature.

With the exception of PVP, other surface-active agents, such as CTAB [120], sodium dodecyl sulfate [121], and sorbitol-alkylamine [122], were also used to synthesize 2D MOF nanomaterials. Surfactant-assisted methods have both benefits and drawbacks for 2D MOF nanomaterials. However, surfactant-assisted methods have the advantages of higher yields and producing ultrathin 2D MOF nanosheets compared to template-assisted and interfacial synthesis methods. Although surfactant-assisted methods yield higher quantities of ultrathin 2D MOF nanosheets compared to template-assisted and interfacial synthesis methods, they also confine the metal on the 2D MOF surface with the surfactant. This restricts the surface metal's activity and limits its utility in catalysis. Therefore, researching ways to automatically deactivate and shed the surfactant post-synthesis in the surfactant-assisted synthesis process could be a productive direction.

Molecular Modulation-Assisted Synthesis

The molecular modulation-assisted method refers to the addition of small molecules that are not ligands and can be coordinated with metal centers to regulate the growth of MOFs. Ma et al. [123] synthesized hexagonal nanoplates (HXPs) by coordinating Ni ions with BDC anions and DABCO (DABCO = 1,4-diazabicyclo[2.2.2]octane), where Ni cations and BDC anions coordinated in-plane to build a 2D architecture, and Ni ions and DABCO molecules formed out-of-plane coordination. The added small pyridine molecule replaced part of the DABCO on the crystal surface (Figure 6a). The pyridine, which has

only one N to coordinate with the Ni ions, inhibited the vertical expansion of the MOF crystals and promoted the formation of a 2D structure with a lateral dimension of 600 to 800 nm (Figure 6b,c) and a thickness of 20 nm (Figure 6d). In addition to pyridine, [124] lauric acid [125] and formic acid [126] can also be employed as molecular regulators to modulate the preparation of MOF nanosheets. For example, lauric acid can modulate the synthesis of MOF crystals by controlling the dispersal rate of organic ligands and metal ions. While molecular modulation-assisted synthesis provides precision in controlling synthetic morphology, it shares a drawback with surfactant-assisted methods—the small molecules that attach to the MOF surface invariably interfere with the activity of the metal. Therefore, optimizing the molecular modulation-assisted synthesis process to allow for the detachment of these molecules during synthesis could present a promising solution.

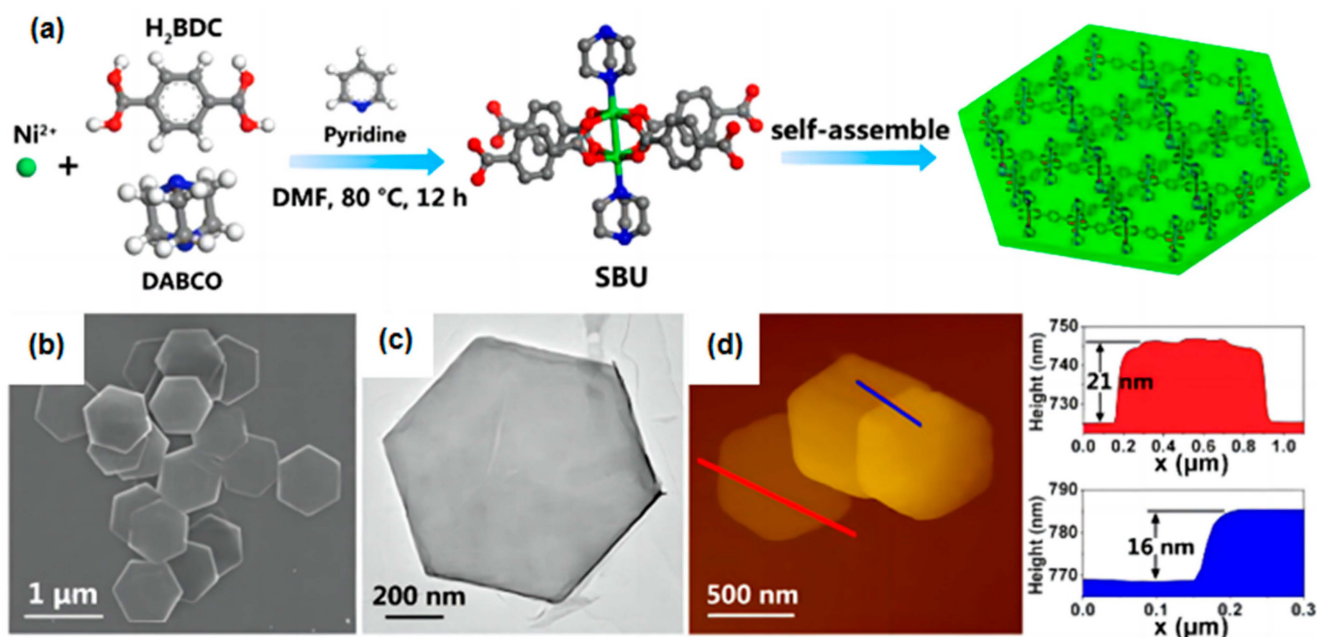


Figure 6. (a) The preparation of HXP. (b) SEM image of HXP. (c) TEM image of HXP. (d) AFM image of HXP. Reproduced with permission [123]. Copyright 2020, American Chemical Society.

Numerous scientists have, so far, unraveled various synthetic strategies for 2D MOFs, primarily falling into two categories: top-down and bottom-up methods. The top-down exfoliation approach is generally straightforward to implement, but it typically yields low output, and the exertion of irregular forces can result in 2D MOFs with uneven morphologies and uncontrollable thickness.

On the other hand, the bottom-up synthesis method allows for control over the morphology and thickness of the synthesized 2D MOFs through the manipulation of growth conditions and reaction environments, thereby improving yield. However, the presence of impurities, such as additives in the reaction, can encapsulate the catalyst surface post-reaction, influencing its performance. Certain restrictive conditions can also impact its applicability, like the limited synthesis space in interfacial synthesis.

Nonetheless, among the various synthesis methods, the bottom-up approach has been gaining increasing interest owing to its ability to control the morphology and thickness and its higher yield efficiency.

2.2. Fabrication Strategy of 2D MOF Derivative

Generally, 2D MOF derivatives can be obtained by simple heating of 2D MOF precursors. The organic ligands of 2D MOFs decompose at appropriate temperatures under different gaseous atmospheres (N_2 , Ar, and Air) to give the corresponding carbonized or oxidized 2D MOF derivatives [127–130]. The generated MOF derivatives generally have ad-

vantages such as high porosity, high specific surface area, high stability, and good electrical conductivity. Additionally, 2D MOFs can be sulfated and phosphorylated to obtain derivatives with high electrocatalytic activity and stability, as shown by Dou et al. [131], who obtained Ni-BDC@NiS derivatives with high OER activity by sulfidation of 2D Ni-BDC.

Although 2D MOF derivatives have many advantages, their preparation has many problems. With the decomposition of organic ligands, the structures of 2D MOFs tend to collapse, leading to the destruction of the original MOF structure. The metal ions in 2D MOFs tend to aggregate, which reduces their activity. Therefore, preparing 2D MOF-derived materials still requires considerable effort from researchers.

Table 1 provides a summary of the prevalent synthetic strategies and methods for creating 2D MOFs and their derivatives. Despite a range of electrocatalysts having been synthesized from these 2D MOFs and their derivatives, the process is not without its flaws. Hence, there is a pressing need for the development of ultra-thin 2D MOFs that feature controllable shape and size coupled with high yield.

Table 1. Synthesis Methods for MOFs and their Composite-Based Electrocatalysts.

2D MOF	Synthesis Method	Synthesis Strategy	Topography	Thickness	Ref.
[Cu ₂ Br(IN) ₂] _n	Top-down Synthesis	Ultrasonic exfoliation	uniform	0.5 ± 0.015 nm	[103]
ZSB-1	Top-down Synthesis	Wet sphere milling/ultrasonic	uniform	11.8 ± 2.3 nm	[104]
vdW MOF-2	Top-down Synthesis	Micro-mechanical peel-off	uneven	10.0 nm	[107]
Zn ₂ (bim) ₃	Top-down Synthesis	Wet sphere milling/ultrasonic	uneven	1.6 nm	[108]
Zn ₂ (PdTCPP)	Top-down Synthesis	Intercalation and chemical exfoliation	uneven	1.0 nm	[109]
[Co(Ni-H7TPPP) ₂] _n ·8H ₂ O	Top-down Synthesis	Chemical exfoliation	uneven	3.9 ± 0.2 nm	[110]
Co ₆ O(dhbdc) ₂	Top-down Synthesis	Electrochemical/chemical exfoliation	wrinkled	2 nm	[111]
ZIF-L	Bottom-up Synthesis	Template assisted	uneven	5.5 μm	[112]
Meso-CuBDC	Bottom-up Synthesis	Sacrificial templates	small square shape	8.0 nm	[113]
Ag ₃ BHT ₂	Bottom-up Synthesis	liquid–liquid interfacial growth	disordered	200 nm	[115]
Ni-MOF	Bottom-up Synthesis	liquid–liquid interfacial growth	uniform	5 nm	[116]
CuBDC	Bottom-up Synthesis	Interfacial synthesis	uniform	5–25 nm	[117]
Zn-TCPP	Bottom-up Synthesis	Surface-active agent-assisted	uniform	7.6 ± 2.6 nm	[118]
Co/Zn-porphyrin	Bottom-up Synthesis	Surfactant-assisted	wrinkled	4–5 nm	[119]
HXP	Bottom-up Synthesis	Molecular modulation assisted	uniform	20 nm	[123]
[Cu(2,5-pydc)(H ₂ O) _n] _n ·2H ₂ O	Bottom-up Synthesis	Ultrasonic exfoliation	uniform	126 nm	[132]
Ni ₃ S ₂ @2D Co-MOF	Bottom-up Synthesis	Self-sacrificial template	rough	60 nm	[133]
NiCoSe	Bottom-up Synthesis	ion-exchange	uniform	230 nm	[134]

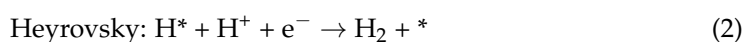
3. Application of 2D MOFs and Their Derivatives for Water Splitting

Due to their tunable structure, rich porosity, and high specific surface area, 2D MOFs and their derivatives have significant promising potential in many areas. Especially in electrocatalysis, their rich porosity facilitates electron transport, and their tunable morphology through metals and ligands makes them effective in water splitting. In particular, 2D MOF derivatives, with their higher conductivity, have excellent performance in electrocatalysis. In the following section, we mainly introduce the application of 2D MOFs and derivatives in water splitting, including HER and OER.

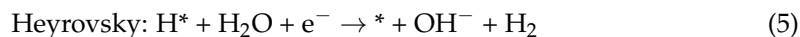
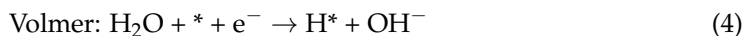
3.1. Hydrogen Evolution Reaction

Hydrogen energy [2,3,135,136] is known to have the highest weight–energy density among all the chemical fuels, and among all the methods to produce hydrogen energy, the electrolysis of water for hydrogen production [8,10,11,137–139] is the most promising in green chemistry because it is an environmentally clean process.

In an acidic solution



In an alkaline or neutral medium



Here, H^* represents the hydrogen atom adsorbed on the catalyst surface, and $*$ represents the active site of the catalyst.

Under acidic conditions, hydrogen ions undergo reduction to form hydrogen, with the equilibrium half-cell potential being 0 V. Meanwhile, under alkaline conditions, water molecules are reduced to produce hydrogen and hydroxyl groups, resulting in an equilibrium half-cell potential of 0.83 V. The HER is a cathodic process involving a two-electron transfer. It has been observed that HER primarily follows either the Volmer–Tafel path or the Volmer–Heyrovsky path, as shown in Equations (1)–(6) [140–145]. HER tends to occur via the Volmer–Tafel path or the Volmer–Heyrovsky path, given in Equations (1)–(6). Note that the only difference between the reaction mechanisms in acidic and basic solutions is the source of protons. The reaction kinetics [146] of HER is related to the experimental Tafel slope [147], where a small Tafel slope indicates that the current density of the hydrogen precipitation reaction increases rapidly as the overpotential increases. The electrochemical HER kinetics are also related to the H_{ad} (surface-bonded H atoms) formed on the electrode surface. If the bonding force between H_{ad} and the electrode is too strong, it will inhibit the Volmer reaction, and if it is too weak, it will inhibit the Heyrovsky reaction or the Tafel reaction. The adsorption Gibbs free energy [148] is usually used to represent the HER performance of the catalyst. As shown in Figure 7, the volcano plot of the HER reaction illustrates the correlation between the free energy of hydrogen binding and the corresponding HER activity of the catalyst. The platinum group metals (Pd [149], Pt [150], Rh [151], and Ir [152]) are positioned near the roof of the volcano and represent the inorganic materials with the best HER properties. The transition metals are positioned to the right of the platinum family metals (such as Ag and Au), which are weakly bonded to hydrogen and difficult to initiate the reaction; the metals located to the left (such as Ni and Co) are more strongly bonded to hydrogen and difficult to release products rapidly.

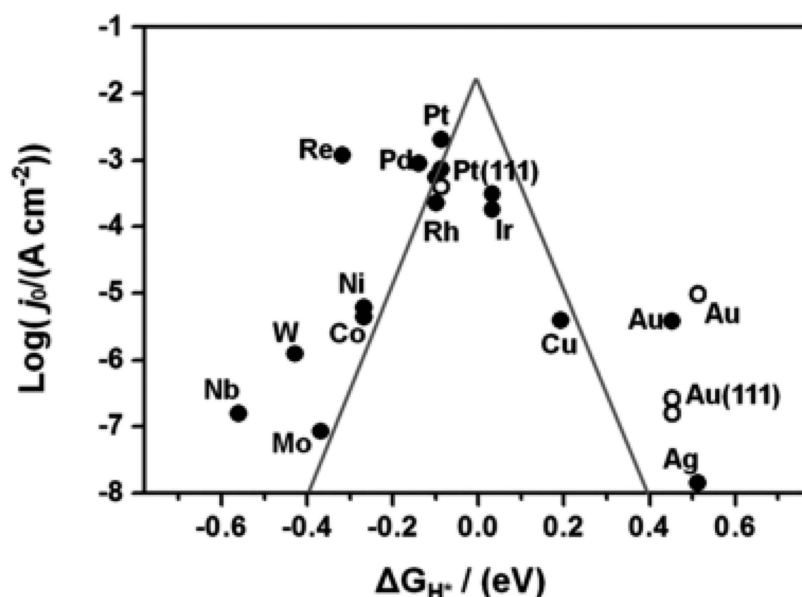


Figure 7. HER Reaction Volcano Diagram [153]. Copyright 2018, Royal Society of Chemistry.

To date, the most advanced HER catalysts are based on a costly precious metal such as Pt [150,154,155] because it has good electrical conductivity, high electrocatalytic activity, and its hydrogen adsorption Gibbs free energy (GH) is close to zero. However, the high cost and severe scarcity greatly impeded the large-scale employment of water electrolysis. In contrast, 2D MOF nanosheets [72,73,75] and their derivatives [82,83,86,87] are novel catalytic materials for HER due to their particular physicochemical properties.

2D MOFs possess highly desirable pore structures with large specific surface areas and controllable morphologies. For example, Daniel Ruiz-Molina et al. [132] successfully prepared thin nanosheets of $[\text{Cu}(2,5\text{-pydc})(\text{H}_2\text{O})]_n \cdot 2\text{H}_2\text{O}$ (pydc = 2,5-pyridinedicarboxylic acid) using ultrasonic exfoliation (Figure 8a), resulting in highly uniform nanosheets with a thickness of approximately 126 nm (Figure 8b,c). Remarkably, the electrocatalytic performance of these nanosheets was significantly enhanced compared to that of the bulk sample, with an overpotential reduced from 530 mV to 340 mV. The improved performance of 2D MOF nanosheets can be attributed to their enhanced electron transfer between the current collector and catalytic sites, which is facilitated by the large surface area and efficient transport pathways in these materials. Using multiple metals in MOF preparation not only optimizes the electronic structure and increases the electrical conductivity but also improves electron transfer and electrocatalytic activity. Cui et al. [156] employed a one-step solvothermal method to prepare NiFe-MOF-74, which exhibited excellent electrocatalytic activity for OER. The hybridized NiFe-MOF-74 showed a network of interconnected honeycomb-like sheets, in contrast to the flower morphology of monometallic Fe-MOF-74 and the spherical shape of Ni-MOF-74 with a diameter of 3–5 μm . This structure provided a large specific surface area, exposure of more metal sites, and facilitated mass transport during the catalytic reaction, driving a current density of -10 mA cm^{-2} requiring only 195 mV overpotential in 1.0 M alkaline solution. As demonstrated in Figure 8d,e, X-ray photoelectron spectroscopy (XPS) images revealed a slightly negative shift of 0.2 eV in the binding energy of Ni 2p $3/2$ in NiFe-MOF-74 and a positive shift of 0.8 eV in the binding energy of Fe 2p $3/2$ in NiFe-MOF-74, indicating that the transfer of electrons from Fe to Ni improved the catalytic activity of the catalyst.

The synthesis of heterostructures in 2D MOF materials has emerged as an effective strategy for enhancing electrocatalytic activity while preserving the previous structure and morphology. For instance, Cheng et al. [133] successfully prepared $\text{Ni}_3\text{S}_2@2\text{D Co-MOF}$ nanosheets by introducing Ni_3S_2 on the surface of Co-MOFs. The resulting $\text{Ni}_3\text{S}_2@2\text{D Co-MOF/CP}$ exhibited remarkable electrocatalytic performance, driving a current density of -10 mA cm^{-2} with an overpotential of only 140 mV in a 1.0 M alkaline solution (Figure 8f). Moreover, the Tafel slope of the material was found to be only 90.3 mV dec^{-1} (Figure 8g), indicating its high catalytic activity and fast electron transfer rate. As shown in Figure 8h,i, the combination of Co-MOFs and Ni_3S_2 can prevent agglomeration on the surface of carbon fibers, and the formation of a honeycomb-like porous structure allows the enhancement of the number of active sites. The XPS pattern demonstrates that the charge transfer from Co-MOF to nickel sulfide enriches its surface with electrons, which promotes H_2 production. Li et al. [157] recently reported that Co-MOF nanosheets were synthesized by the hydrothermal process. Then, 2D CoP/Co-MOF heterostructure nanosheets were prepared by low-temperature phosphorylation on a carbon paper substrate. The prepared CoP/Co-MOF has a similar 2D nanosheet structure as the pristine Co-MOF. The TEM and SEM outcomes indicate that the 2D CoP/MOF heterostructure was fabricated successfully by partly phosphorylation, which has a larger surface area and exposes more active sites. The electrostatic interactions between the 2D CoP nanosheets and 2D Co-MOF nanosheets play a crucial role in modulating the surface chemistry of the resulting electrocatalysts. Specifically, the 2D CoP/Co-MOF nanosheet array exhibits exceptional electrocatalytic performance, requiring only an overpotential of 52 mV to drive a current density of -10 mA cm^{-2} in 0.5 M H_2SO_4 . CoP/Co-MOF heterostructures can thoroughly combine the superior electrical conductivity and porosity of Co-based nanoparticles and the original

MOF's advantage of dispersed active sites. In catalysts that form heterojunctions, the activity of the catalyst is improved due to the modification of the electronic morphology.

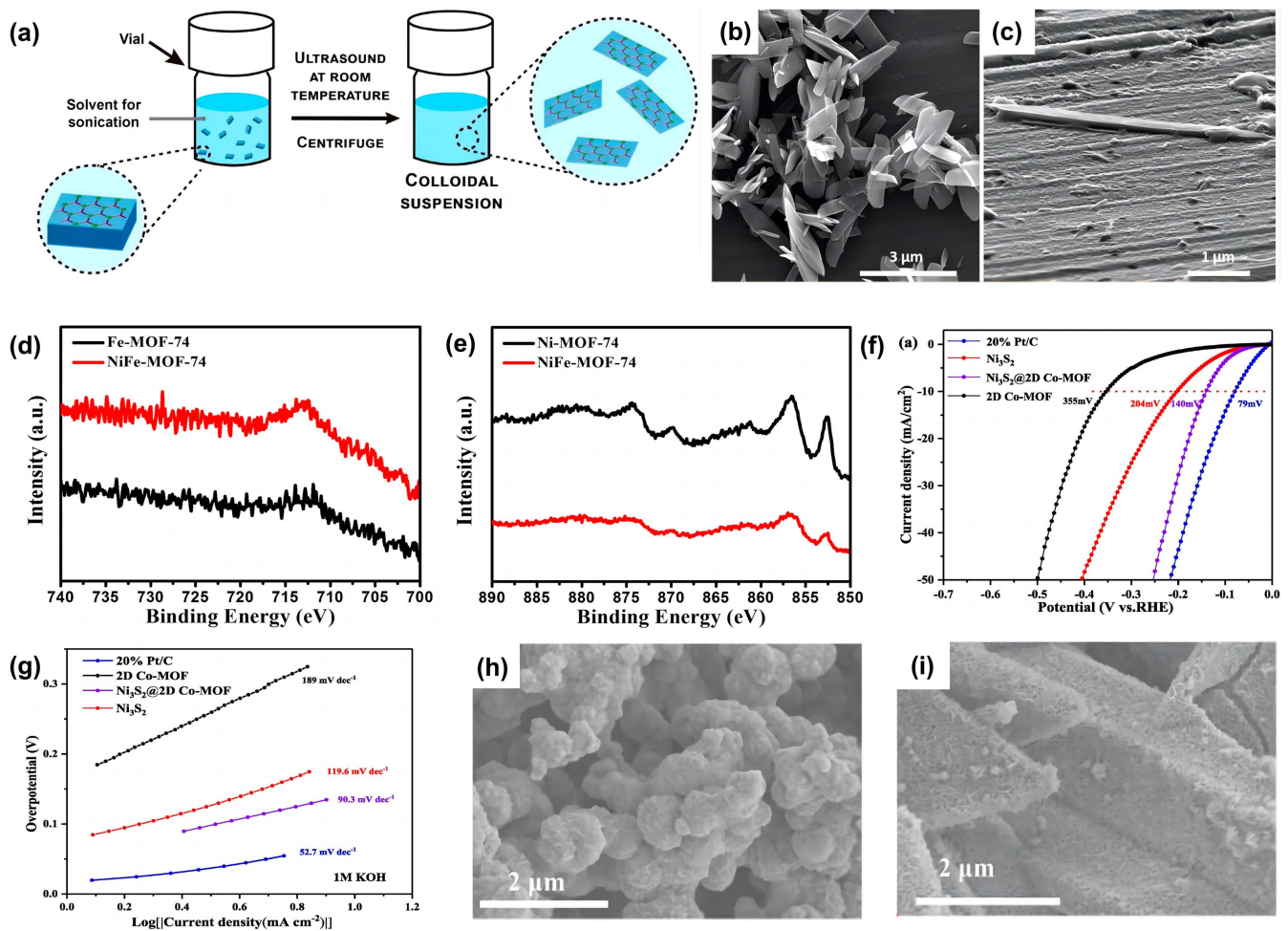


Figure 8. (a) Ultrasound-assisted exfoliation process of $[\text{Cu}(2,5\text{-pydc})(\text{H}_2\text{O})]_n \cdot 2\text{H}_2\text{O}$. (b) SEM image of the exfoliated nanosheets. (c) SEM image of nanosheets. (d) XPS spectra of Fe 2p. (e) XPS spectra of Ni 2p. Reproduced with permission. [132,156] Copyright 2021, Elsevier. (f) $\text{Ni}_3\text{S}_2@2\text{D Co-MOF}/\text{CP}$ polarization curves. (g) Tafel plots of $\text{Ni}_3\text{S}_2@2\text{D Co-MOF}/\text{CP}$. (h) SEM images of $\text{Ni}_3\text{S}_2/\text{CP}$. (i) SEM images of $\text{Ni}_3\text{S}_2@2\text{D Co-MOF}/\text{CP}$. Reproduced with permission [133]. Copyright 2022, Elsevier.

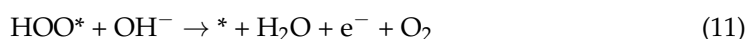
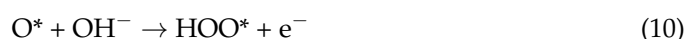
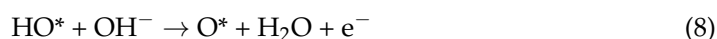
In addition, Yang et al. [134] fabricated 2D MOF-derived multiporous NiCoSe nanosheet arrays based on ZIF-67. NiCoSe nanosheet arrays drive a current density of -10 mA cm^{-2} , requiring only 170 mV low overpotential in alkaline solutions; the outstanding HER electrocatalytic performance of NiCoSe was attributed to the porous structure, exposing more active sites. Kim et al. [158] synthesized a novel mesoporous bimetallic sulfide combined CoS_2 nanoarray mixture $\text{FeS}_2\text{-MoS}_2@2\text{D Co-MOF}$ by designing and utilizing 2D MOF-derived materials. This catalyst drove a current density of -10 mA cm^{-2} requiring only 92 mV overpotential in 1.0 M alkaline solution. By combining MoS_2 with FeS_2 sheets, additional active sites were generated, and conductivity was enhanced, resulting in improved intrinsic performance for the HER. Table 2 summarizes the HER catalytic performance of various 2D MOFs and their derivatives.

3.2. Oxygen Evolution Reaction

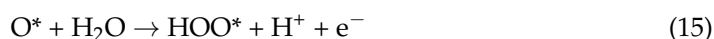
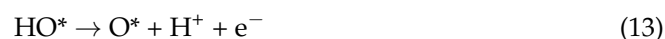
The water electrolysis reaction device mainly comprises two half-reactions, the anode [16,17] OER, and the cathode HER. Compared with the HER, the OER involving four-electron transfer has slow kinetics. The standard electrode potential of the OER on

the anode is 1.23 V, and the standard electrode potential of the HER on the cathode is 0 V, so the minimum theoretical voltage required for the overall reaction of water electrolysis is 1.23V [159–162]. Under acidic conditions, the oxidation of two water molecules yields four hydrogen ions and one molecule of oxygen, with the equilibrium half-cell potential established at 1.23V. Conversely, in alkaline conditions, the oxidation of four hydroxide groups produces two water molecules and one molecule of oxygen, resulting in an equilibrium half-cell potential of 0.404V. The OER occurring at the anode is a four-electron transfer reaction process, which is dynamically slow. Thus, the OER often requires overcoming a larger energy obstacle to drive the reaction. Therefore, the key to reducing the cost of hydrogen production and the power consumption for large-scale water splitting is to effectively decrease the overpotential of the OER at the anode [163–168] to achieve high-current hydrogen production at low pressure.

In an alkaline



In an acidic solution



where * represents the active site of the catalyst.

OER is a crucial half-reaction that takes place at the anode during water splitting, and its mechanism can vary depending on whether the reaction occurs in acidic or alkaline conditions [16,169–172]. Currently, the precise mechanism of OER is not fully understood, and researchers have proposed several potential mechanisms. Among them, the most widely accepted view is that the intermediate M-OH or M-O is formed during OER. Subsequently, these intermediates can follow two routes: the vertical path (shown in Figure 9), where the M-O intermediate directly combines to generate O₂, and the left semicircular route (also depicted in Figure 9), where the M-O intermediate further transforms into the M-OOH intermediate, which subsequently decomposes to release O₂. These pathways are illustrated by Equations (7)–(16).

Traditionally, catalysts based on noble metals such as IrO_x exhibit higher activity for oxygen production. However, due to their scarcity, high cost, and susceptibility to deactivation, water electrolysis technologies employing precious metal catalysts are not widely utilized. With the advancement of 2D MOF materials, an increasing number of 2D MOFs have shown promising activity in OER. The catalytic performance of 2D MOF

materials in OER [173–176] has garnered significant attention, offering potential alternatives to noble metal catalysts.

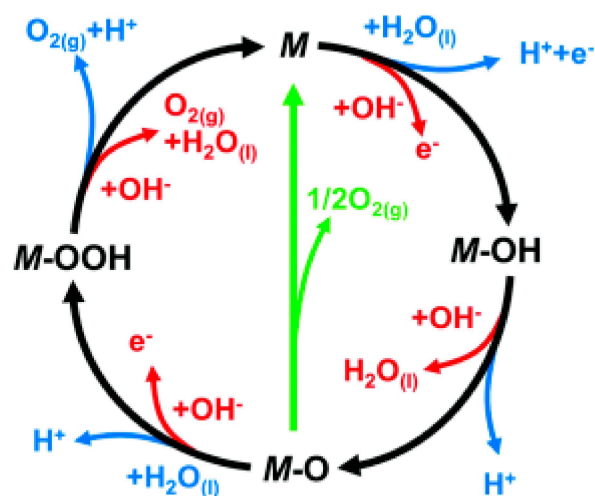


Figure 9. Mechanism of OER [177]. Copyright 2018, Springer Nature.

The 2D MOFs are layered materials composed of organic ligands and metal ions, and the catalytic activity of bimetallic 2D MOFs can be enhanced due to the synergistic interaction between the bimetallic atoms. Peng et al. [178] synthesized NiCo-MOF by a one-step hydrothermal procedure. Figure 10a,b shows that introducing Ni into 2D ZIF-67 not only reduces agglomeration but also promotes the formation of 2D lamellar structures. As demonstrated in Figure 10c,d, XPS analysis revealed that the 5% NiCo-MOF exhibited a higher Co 2p binding energy compared to the 2D ZIF-67, with peaks observed at 796.7 and 781.2 eV, respectively. This indicates that the addition of Ni can modulate the electronic arrangement of Co and change its chemical valence so that it can attract electrons more efficiently, thus improving the catalytic performance and accelerating the charge transfer. The electrocatalytic activity of the 5% NiCo-MOF can be optimized by adjusting the molar ratio of Ni/Co. By doing so, the material was found to achieve an impressive η value, driving a current density of 10 mA cm^{-2} with an overpotential of only 310 mV. Zhu [179] added triethylamine to promote MOF nanosheet synthesis and prepared 2D MOF-Fe/Co by simple stirring at room temperature. The MOF-Fe/Co (1:2) exhibits outstanding electrocatalytic performance, with a low overpotential of only 238 mV required to achieve a current density of 10 mA cm^{-2} in an alkaline solution. Additionally, it has a low Cdl value of 66.9 mF cm^2 , indicating its high electrocatalytic activity and fast electron transfer rate. Zhu [180] used bimetallic LDH nanomaterials as a sacrificial template to prepare 2D NiFe MOF, as shown in Figure 10e,f, and the width of the prepared NiFe MOF was approximately $0.4\text{--}0.6 \mu\text{m}$ in 2D planar nanosheets. The prepared MOFs possess the activity sites for oxygen evolution, bimetallic components, and coordination environment from LDHs. The carboxylated organic ligands can be used as intermediates to transfer protons due to their ability to ionize hydrogen ions, which improves the proton transfer efficiency and OH adsorption of 2D MOF nanosheets. The freestanding NiFe-2D MOF nanosheets drive a current density of 10 mA cm^{-2} , requiring only 260 mV overpotential (Figure 10g). When nickel foam is used to fabricate LDH nanosheets, the overvoltage is even as low as 221 mV.

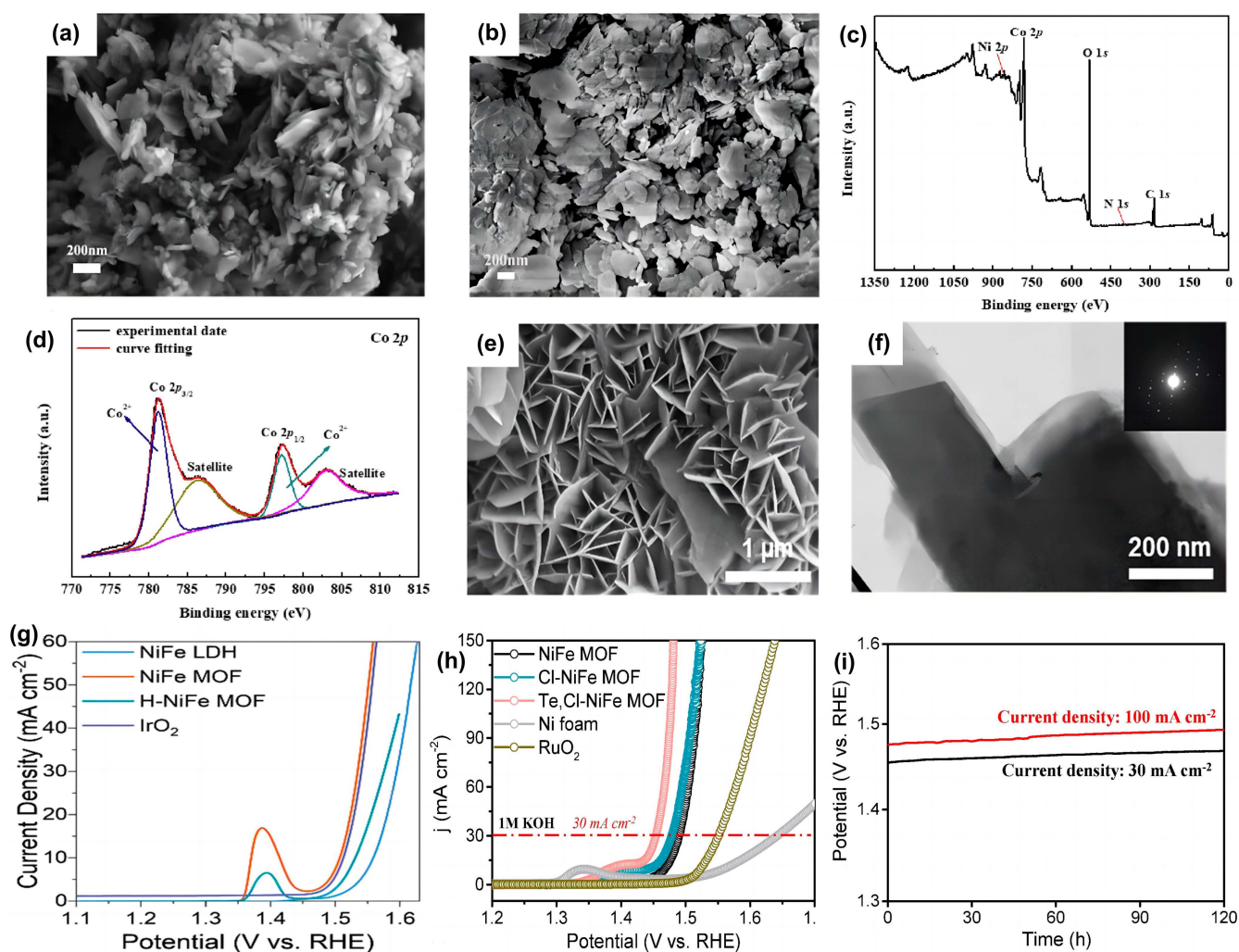


Figure 10. (a) SEM of 2D ZIF-67. (b) SEM of 5% NiCo-MOF. (c) XPS spectra of 5% NiCo-MOF. (d) XPS spectra of Co 2p. Reproduced with permission. [178] Copyright 2021, Elsevier. (e) SEM image of NiFe MOF nanosheets. (f) TEM image of NiFe MOF nanosheets. (g) LSV plots of NiFe MOF for OER. Reproduced with permission. [180] Copyright 2022, Wiley-VCH. (h) Te,Cl-NiFe MOF polarization curves. (i) Te,Cl-NiFe MOF electrochemical stability. Reproduced with permission [181] Copyright 2022, Elsevier.

The introduction of metalloids in MOFs regulates the electronic structure and increases the electrical conductivity. The introduction of non-metallic elements in MOFs can create atomic vacancies and defects and increase additional active sites in catalytic reactions. Song [181] prepared Te,Cl-NiFe MOF by introducing Cl and Te elements into the NiFe MOF, which exhibited uniform 2D nanosheets. The participation of Te elements in the MOF facilitates the transport of electrons from Fe to Te and improves the kinetics of the reaction. In contrast, the participation of halogenated elements promotes the oxidation of Cl due to the larger electronegativity of Cl atoms, which can induce more active sites. Thus, the Cl and Te co-doped NiFe MOFs grown on nickel foam demonstrated remarkable OER performance, achieving a current density of 30 mA cm^{-2} with an overpotential of only 224 mV (Figure 10h). Furthermore, these materials displayed exceptional long-term stability, maintaining their activity for over 120 h (Figure 10i).

The 2D MOFs can be obtained as derivatives by appropriate treatment, and their morphology can be kept the same as the previous. Yang et al. [182] designed and synthesized $\text{FeNi}_3\text{-Fe}_3\text{O}_4$ hierarchical nanoparticles homogeneously immobilized on carbon nanotubes and MOF nanosheets ($\text{FeNi}_3\text{-Fe}_3\text{O}_4$ NPs/MOF-CNT). Due to the 3D multiporous nanos-

structure of the MOF precursor and the modification of the electronic configuration of Ni by Fe₃O₄, the FeNi₃-Fe₃O₄ NPs/MOF-CNT drives a current density of 10 mA cm⁻² requiring only 234 mV overpotential, while the slope of Tafel is 37.0 mV dec⁻¹.

Cao [183] used 2D Co-TCPP (Fe) MOF as a precursor to obtaining MOF-derived Fe-CoP/C composite nanoplatelets by high-temperature carbonization and phosphorylation of carbon cloth. This Fe-CoP/C composite drives a current density of 10 mA cm⁻² requiring 290 mV overpotential in 1 M KOH. The added Fe can regulate the electronic structure of CoP and the 2D morphology derived from MOF. The conductive network formed by the carbon substrate can increase the electron transfer efficiency and optimize the sample performance. Table 3 summarizes the OER catalytic properties of the 2D MOFs and their derivatives.

Table 2. 2D MOFs and their derivative electrocatalysts for HER (η : overpotential at 10 mA cm⁻², if not specified).

Catalyst Name	Type	Electrolyte	η [mV]	Tafel Slope [mV dec ⁻¹]	Ref.
[Cu(2,5-pydc)(H ₂ O)] _n ·2H ₂ O NSs	2D MOFs	1.0 M KOH	340	70	[132]
NiFe-MOF-74	2D MOFs	1.0 M KOH	195	136	[156]
Ni ₃ S ₂ @2D Co-MOF/CP	2D MOFs	1.0 M KOH	140	90.3	[133]
2D CoP/Co-MOF	2D MOFs derivatives	0.5 M H ₂ SO ₄	52	49	[157]
		1.0 M KOH	26	53	
NiCoSe	2D MOFs derivatives	1.0 M PBS	106	89	[134]
		1.0 M KOH	170	82.3	
FeS ₂ -MoS ₂ @CoS ₂ -MOF	2D MOFs derivatives	1.0 M KOH	92	70.4	[158]
FeNi ₃ -Fe ₃ O ₄ NPs/MOF-CNT	2D MOFs derivatives	1.0 M KOH	108	96.7	[182]
CCS-NiFeP	2D MOFs derivatives	1.0 M KOH	56	38	[184]
Ni/Ni ₃ S ₂ @CN	2D MOFs derivatives	1.0 M KOH	141	91	[185]
		0.5 M H ₂ SO ₄	187	83	
Ce-MOF@Pt	2D MOFs	1.0 M KOH	208	188.1	[186]
		1.0 M KOH	33	34	
Pt@CuFe-LDHm	2D MOFs derivatives	0.1 M KOH	47	50.2	[187]
		1.0 M PBS	120	85.6	
Fe-NiS/MoS ₂	2D MOFs derivatives	1.0 M KOH	120	69	[188]
Ni@CoO@CoMOFC	2D MOFs derivatives	1.0 M KOH	138	59	[189]
CoNiP/NF	2D MOFs derivatives	1.0 M KOH	147	51	[190]
TS-Co ₃ O ₄ @VS ₂	2D MOFs derivatives	0.5 M H ₂ SO ₄	175.2	57	[191]

Table 3. 2D MOFs and their derivative electrocatalysts for OER (η : overpotential at 10 mA cm⁻², if not specified).

Catalyst Name	Type	Electrolyte	η [mV]	Tafel Slope [mV dec ⁻¹]	Ref.
NiFe-MOF-74	2D MOFs	1.0 m KOH	208	54	[156]
NiCoSe	2D MOFs derivatives	1.0 M KOH	278 [20 mA cm ⁻²]	92	[134]
FeS ₂ -MoS ₂ @CoS ₂ -MOF	2D MOFs derivatives	1.0 M KOH	211 [20 mA cm ⁻²]	64.5	[158]
NiCo-MOF	2D MOFs	1.0 M KOH	310	106.3	[178]
2D MOF-Fe/Co	2D MOFs	1.0 M KOH	238	52	[179]
NiFe MOF/NF	2D MOFs	1.0 M KOH	221	40	[180]
Te,Cl-NiFe MOF	2D MOFs derivatives	1.0 M KOH	224 [30 mA cm ⁻²]	37.6	[181]
FeNi ₃ -Fe ₃ O ₄ NPs/MOF-CNT	2D MOFs derivatives	1.0 M KOH	234	37	[182]
Fe-CoP/C	2D MOFs derivatives	1.0 M KOH	290	50	[183]
Ce-MOF@Pt	2D MOFs	1.0 M KOH	340	47.9	[186]
Fe-NiS/MoS ₂	2D MOFs derivatives	1.0 M KOH	297	54.7	[188]
NiFe-BTC/CCHH/NF	2D MOFs derivatives	1.0 M KOH	270 [50 mA cm ⁻²]	/	[192]
Ni@CoO@CoMOFC	2D MOFs derivatives	1.0 M KOH	247	51	[189]
CoNiP/NF	2D MOFs derivatives	1.0 M KOH	234	47	[190]
Ru-NiFeP/NF	2D MOFs derivatives	1.0 M KOH	179	44.9	[193]

Water splitting encompasses both HER and OER. While most 2D MOF catalysts exhibit excellent performance in OER, their performance in HER tends to be relatively subpar. This underscores the need to develop bifunctional catalysts demonstrating high performance in both HER and OER. A prime example of such a bifunctional catalyst is the NiFe-MOF-74, synthesized by Cui et al. [156] through a one-step hydrothermal method. This catalyst requires only 1.58 V to generate 10 mA cm⁻² of current. In a separate study, Kim et al. [158] synthesized a unique hybrid catalyst, FeS₂-MoS₂@CoS₂-MOF, that required only 1.58 V, 1.66 V, and 1.78 V to generate 10, 50, and 100 mA cm⁻² of current, respectively. While some bifunctional catalysts may not match the high performance of single-function catalysts, they can substantially simplify the reaction apparatus in the context of electrocatalytic water splitting. Given these benefits, it is evident that increased research focus on bifunctional catalysts is warranted.

4. Summary and Outlook

In conclusion, this study provides a comprehensive review of various synthesis methods employed in the preparation of 2D MOFs and their derivatives, with a specific focus on their applications in electrocatalytic hydrolysis. Despite significant advancements made in recent years, 2D MOFs and their derivatives in electrocatalysis continue to be an intriguing research area that is anticipated to attract increased attention. On the whole, 2D MOFs and their derivatives are emerging as particularly promising electrocatalysts due to several distinguishing properties. Primarily, the unique structure of 2D MOFs affords them efficient ion transport and electron transfer capabilities. In addition, 2D MOFs possess a vast active surface area and myriad active sites, facilitating the absorption of hydrogen ions. Furthermore, the selectable nature of metal ions and ligands presents a plethora of potential structural combinations, allowing for the design and synthesis of 2D MOFs with controllable morphology. The introduction of varied functional groups via different ligands can also enhance catalytic performance in diverse ways, thereby adding another layer of versatility to these advanced materials. This review highlights several opportunities and challenges associated with MOFs and their derivatives in electrocatalysis and provides outlook and perspectives for future research:

(1) Both top-down and bottom-up synthesis methods come with their inherent drawbacks. While the top-down approach offers simplicity, it is often marred by inconsistent results and a low yield. Conversely, the bottom-up synthesis method may be influenced by solvents and other added materials during the synthesis process. Identifying and overcoming these limitations, as well as finding ways to mitigate adverse effects on 2D MOF materials, will play a pivotal role in enhancing their performance.

(2) 2D MOFs, with their rich porosity, tunable structures, and high specific surface areas, hold promise in enhancing catalytic performance. However, their low conductivity and stability need to be addressed. Therefore, there is a need to develop more stable and conductive 2D MOF materials. Exploring the change in electronic configuration between the ligand and the central atom in 2D MOFs can provide insights for designing structures with higher electron transfer rates and improved stability.

(3) The substantial cost of certain organic ligands used in the synthesis of 2D MOFs presents a significant obstacle to their broad application. The development of cost-effective ligands is of utmost importance for the design of efficient 2D MOF catalysts that are suitable for practical usage.

(4) Despite the superior benefits that 2D MOF derivatives bring compared to 2D MOFs, complications such as the collapse of porous structures and agglomeration of metal particles during the carbonization process can notably compromise their performance. Therefore, a heightened focus on the detailed changes that occur during the carbonization process and the development of more efficient synthesis methods to maintain the desirable attributes is imperative.

(5) Organic ligands encompass a wide variety of functional groups, each with different electron-donating abilities and potential contributions to the catalytic performance and

stability of 2D MOFs after coordination. Furthermore, some organic ligands featuring specific functional groups have the capability to bind with hydrogen ions. This characteristic facilitates their absorption of hydrogen ions from aqueous solutions, making it easier for the ions to transfer to metal ions at active sites. This process inherently enhances the performance of the catalysts. However, there is limited research in this area. Exploring 2D MOFs and their composites with different functional groups holds considerable potential for tailoring their properties and enhancing their catalytic performance and stability.

(6) While numerous 2D MOFs and their derivatives have been investigated in electrocatalysis, there are still unresolved questions regarding the underlying catalytic mechanisms in the electrocatalytic process. Further research is needed to gain a better understanding of these mechanisms by employing advanced in situ characterization techniques in conjunction with density functional theory results.

Overall, the development of 2D MOFs and their derivatives as efficient electrocatalysts represents a promising area of research with substantial potential to contribute to the transition towards a more sustainable energy system. Continued exploration and advancements in this field will undoubtedly pave the way for the design of novel catalysts with enhanced performance and broad applications in various electrochemical processes.

Author Contributions: L.S. was involved in the conception, investigation, design, and writing of both the original draft and the review and editing stages. Y.Q. and Z.L. took part in writing the original draft, in addition to the review and editing process. D.-H.K. and D.J.K. made significant contributions to the conception, project management, supervision, design, and writing of the original draft and the review and editing phases. All authors have read and agreed to the published version of the manuscript.

Funding: This work was supported by a National Research Foundation of Korea (NRF) grant funded by the Korean government (2021R1A2C2012127).

Conflicts of Interest: The authors declare that they have no known competing financial interest or personal relationships that could have appeared to influence the work reported in this paper.

References

1. Egeland-Eriksen, T.; Hajizadeh, A.; Sartori, S. Hydrogen-based systems for integration of renewable energy in power systems: Achievements and perspectives. *Int. J. Hydrogen Energy* **2021**, *46*, 31963–31983. [[CrossRef](#)]
2. Dawood, F.; Anda, M.; Shafiullah, G.M. Hydrogen production for energy: An overview. *Int. J. Hydrogen Energy* **2020**, *45*, 3847–3869. [[CrossRef](#)]
3. Ahmed, A.; Al-Amin, A.Q.; Ambrose, A.F.; Saidur, R. Hydrogen fuel and transport system: A sustainable and environmental future. *Int. J. Hydrogen Energy* **2016**, *41*, 1369–1380. [[CrossRef](#)]
4. Xu, X.; Shao, Z.; Jiang, S.P. High-Entropy Materials for Water Electrolysis. *Energy Technol.* **2022**, *10*, 2200573.
5. Xu, X.; Pan, Y.; Ge, L.; Chen, Y.; Mao, X.; Guan, D.; Li, M.; Zhong, Y.; Hu, Z.; Peterson, V.K.; et al. High-performance perovskite composite electrocatalysts enabled by controllable interface engineering. *Small* **2021**, *17*, e2101573. [[CrossRef](#)] [[PubMed](#)]
6. Tang, J.; Xu, X.; Tang, T.; Zhong, Y.; Shao, Z. Perovskite-Based Electrocatalysts for Cost-Effective Ultrahigh-Current-Density Water Splitting in Anion Exchange Membrane Electrolyzer Cell. *Small Methods* **2022**, *6*, 2201099. [[CrossRef](#)]
7. Anantharaj, S.; Noda, S. Amorphous Catalysts and Electrochemical Water Splitting: An Untold Story of Harmony. *Small* **2020**, *16*, e1905779. [[CrossRef](#)]
8. Xu, H.; Zhao, Y.; He, G.; Chen, H. Race on engineering noble metal single-atom electrocatalysts for water splitting. *Int. J. Hydrogen Energy* **2022**, *47*, 14257–14279. [[CrossRef](#)]
9. Guo, C.; Shi, Y.; Lu, S.; Yu, Y.; Zhang, B. Amorphous nanomaterials in electrocatalytic water splitting. *Chin. J. Catal.* **2021**, *42*, 1287–1296. [[CrossRef](#)]
10. You, B.; Tang, M.T.; Tsai, C.; Abild-Pedersen, F.; Zheng, X.; Li, H. Enhancing Electrocatalytic Water Splitting by Strain Engineering. *Adv. Mater.* **2019**, *31*, e1807001. [[CrossRef](#)]
11. Yang, X.; Guo, R.; Cai, R.; Ouyang, Y.; Yang, P.; Xiao, J. Engineering high-entropy materials for electrocatalytic water splitting. *Int. J. Hydrogen Energy* **2022**, *47*, 13561–13578. [[CrossRef](#)]
12. Verma, J.; Goel, S. Cost-effective electrocatalysts for Hydrogen Evolution Reactions (HER): Challenges and Prospects. *Int. J. Hydrogen Energy* **2022**, *47*, 38964–38982. [[CrossRef](#)]
13. Pan, Y.; Zhang, C.; Lin, Y.; Liu, Z.; Wang, M.; Chen, C. Electrocatalyst engineering and structure-activity relationship in hydrogen evolution reaction: From nanostructures to single atoms. *Sci. China Mater.* **2020**, *63*, 921–948. [[CrossRef](#)]

14. Baek, D.S.; Lee, J.; Lim, J.S.; Joo, S.H. Nanoscale electrocatalyst design for alkaline hydrogen evolution reaction through activity descriptor identification. *Mater. Chem. Front.* **2021**, *5*, 4042–4058. [[CrossRef](#)]
15. Zeng, F.; Mebrahtu, C.; Liao, L.; Beine, A.K.; Palkovits, R. Stability and deactivation of OER electrocatalysts: A review. *J. Energy Chem.* **2022**, *69*, 301–329. [[CrossRef](#)]
16. Zubair, M.; Hassan, M.M.U.; Mehran, M.T.; Baig, M.M.; Hussain, S.; Shahzad, F. 2D MXenes and their heterostructures for HER, OER and overall water splitting: A review. *Int. J. Hydrogen Energy* **2022**, *47*, 2794–2818. [[CrossRef](#)]
17. Zhang, K.; Zou, R. Advanced Transition Metal-Based OER Electrocatalysts: Current Status, Opportunities, and Challenges. *Small* **2021**, *17*, e2100129.
18. Raeisi-Kheirabadi, N.; Nezamzadeh-Ejhieh, A.; Aghaei, H. Electrochemical amperometric sensing of loratadine using NiO modified paste electrode as an amplified sensor. *Iran. J. Catal.* **2021**, *11*, 181–189.
19. Tamiji, T.; Nezamzadeh-Ejhieh, A. Electrocatalytic behavior of AgBr NPs as modifier of carbon past electrode in the presence of methanol and ethanol in aqueous solution: A kinetic study. *J. Taiwan Inst. Chem. Eng.* **2019**, *104*, 130–138. [[CrossRef](#)]
20. Qian, Y.; Yu, J.; Lyu, Z.; Zhang, Q.; Lee, T.H.; Pang, H.; Kang, D.J. Durable hierarchical phosphorus-doped biphasic MoS₂ electrocatalysts with enhanced H⁺ adsorption. *Carbon Energy* **2023**, e376. [[CrossRef](#)]
21. Qian, Y.; Du, J.; Kang, D.J. Enhanced electrochemical performance of porous Co-doped TiO₂ nanomaterials prepared by a solvothermal method. *Microporous Mesoporous Mater.* **2019**, *273*, 148–155. [[CrossRef](#)]
22. Liu, M.; Zhang, C.; Han, A.; Wang, L.; Sun, Y.; Zhu, C.; Li, R.; Ye, S. Modulation of morphology and electronic structure on MoS₂-based electrocatalysts for water splitting. *Nano Res.* **2022**, *15*, 6862–6887. [[CrossRef](#)]
23. Wang, M.; Zhang, L.; Pan, J.; Huang, M.; Zhu, H. A highly efficient Fe-doped Ni₃S₂ electrocatalyst for overall water splitting. *Nano Res.* **2021**, *14*, 4740–4747. [[CrossRef](#)]
24. Pang, Y.; Xu, W.; Zhu, S.; Cui, Z.; Liang, Y.; Li, Z.; Wu, S.; Chang, C.; Luo, S. Self-supporting amorphous nanoporous NiFeCoP electrocatalyst for efficient overall water splitting. *J. Mater. Sci. Technol.* **2021**, *82*, 96–104. [[CrossRef](#)]
25. Huang, L.; Yao, R.; Wang, X.; Sun, S.; Zhu, X.; Liu, X.; Kim, M.G.; Lian, J.; Liu, F.; Li, Y.; et al. In situ phosphating of Zn-doped bimetallic skeletons as a versatile electrocatalyst for water splitting. *Energy Environ. Sci.* **2022**, *15*, 2425–2434. [[CrossRef](#)]
26. Wang, Y.; Sun, Y.; Yan, F.; Zhu, C.; Gao, P.; Zhang, X.; Chen, Y. Self-supported NiMo-based nanowire arrays as bifunctional electrocatalysts for full water splitting. *J. Mater. Chem. A* **2018**, *6*, 8479–8487.
27. Yu, X.; Guo, J.; Li, B.; Xu, J.; Gao, P.; Hui, K.S.; Hui, K.N.; Shao, H. Sub-Nanometer Pt Clusters on Defective NiFe LDH Nanosheets as Trifunctional Electrocatalysts for Water Splitting and Rechargeable Hybrid Sodium–Air Batteries. *ACS Appl. Mater. Interfaces* **2021**, *13*, 26891–26903. [[CrossRef](#)]
28. Peng, J.; Tao, P.; Song, C.; Shang, W.; Deng, T.; Wu, J. Structural evolution of Pt-based oxygen reduction reaction electrocatalysts. *Chin. J. Catal.* **2022**, *43*, 47–58. [[CrossRef](#)]
29. Qian, Y.; Yu, J.; Zhang, Y.; Zhang, F.; Kang, Y.; Su, C.; Shi, H.; Kang, D.J.; Pang, H. Interfacial microenvironment modulation enhancing catalytic kinetics of binary metal sulfides heterostructures for advanced water splitting electrocatalysts. *Small Methods* **2022**, *6*, 2101186. [[CrossRef](#)]
30. Liu, H.; Xi, C.; Xin, J.; Zhang, G.; Zhang, S.; Zhang, Z.; Huang, Q.; Li, J.; Liu, H.; Kang, J. Free-standing nanoporous NiMnFeMo alloy: An efficient non-precious metal electrocatalyst for water splitting. *Chem. Eng. J.* **2021**, *404*, 126530. [[CrossRef](#)]
31. Lu, S.; Zhang, Y.; Lou, F.; Guo, K.; Yu, Z. Non-precious metal activated MoSi₂N₄ monolayers for high-performance OER and ORR electrocatalysts: A first-principles study. *Appl. Surf. Sci.* **2022**, *579*, 152234. [[CrossRef](#)]
32. Rojas, S.; Rodríguez-Diéguez, A.; Horcajada, P. Metal–Organic Frameworks in Agriculture. *ACS Appl. Mater. Interfaces* **2022**, *14*, 16983–17007. [[CrossRef](#)] [[PubMed](#)]
33. Zhou, S.; Lu, L.; Liu, D.; Wang, J.; Sakiyama, H.; Muddassir, M.; Nezamzadeh-Ejhieh, A.; Liu, J. Series of highly stable Cd(II)-based MOFs as sensitive and selective sensors for detection of nitrofurantoin antibiotic. *CrystEngComm* **2021**, *23*, 8043–8052. [[CrossRef](#)]
34. Qian, Y.; Zhang, F.; Kang, D.J.; Pang, H. A review of metal–organic framework-based compounds for environmental applications. *Energy Environ. Mater.* **2023**, *6*, 12414. [[CrossRef](#)]
35. Rao, C.; Liao, D.; Pan, Y.; Zhong, Y.; Zhang, W.; Ouyang, Q.; Nezamzadeh-Ejhieh, A.; Liu, J. Novel formulations of metal-organic frameworks for controlled drug delivery. *Expert Opin. Drug Deliv.* **2022**, *19*, 1183–1202. [[CrossRef](#)]
36. Chen, J.; Cheng, F.; Luo, D.; Huang, J.; Ouyang, J.; Nezamzadeh-Ejhieh, A.; Khan, M.S.; Liu, J.; Peng, Y. Recent advances in Ti-based MOFs in biomedical applications. *Dalton Trans.* **2022**, *51*, 14817–14832. [[CrossRef](#)]
37. Nicks, J.; Sasitharan, K.; Prasad, R.R.R.; Ashworth, D.J.; Foster, J.A. Metal–Organic Framework Nanosheets: Programmable 2D Materials for Catalysis, Sensing, Electronics, and Separation Applications. *Adv. Funct. Mater.* **2021**, *31*, 2103723. [[CrossRef](#)]
38. Xu, X.; Sun, H.; Jiang, S.P.; Shao, Z. Modulating metal–organic frameworks for catalyzing acidic oxygen evolution for proton exchange membrane water electrolysis. *Susmat* **2021**, *1*, 460–481. [[CrossRef](#)]
39. Qian, Y.; Zhang, F.; Zhao, S.; Bian, C.; Mao, H.; Kang, D.J.; Pang, H. Recent progress of metal-organic framework-derived composites: Synthesis and their energy conversion applications. *Nano Energy* **2023**, *111*, 108415. [[CrossRef](#)]
40. Liu, J.; Song, X.; Zhang, T.; Liu, S.; Wen, H.; Chen, L. 2D Conductive Metal–Organic Frameworks: An Emerging Platform for Electrochemical Energy Storage. *Angew. Chem. Int. Ed.* **2021**, *60*, 5612–5624. [[CrossRef](#)]
41. Qian, Y.; Lyu, Z.; Zhang, Q.; Lee, T.H.; Kang, T.K.; Sohn, M.; Shen, L.; Kim, D.H.; Kang, D.J. High-Performance Flexible Energy Storage Devices Based on Graphene Decorated with Flower-Shaped MoS₂ Heterostructures. *Micromachines* **2023**, *14*, 297. [[CrossRef](#)] [[PubMed](#)]

42. Wang, J.-X.; Yin, J.; Shekhah, O.; Bakr, O.M.; Eddaoudi, M.; Mohammed, O.F. Energy Transfer in Metal–Organic Frameworks for Fluorescence Sensing. *ACS Appl. Mater. Interfaces* **2022**, *14*, 9970–9986. [[CrossRef](#)] [[PubMed](#)]
43. Olorunyomi, J.F.; Geh, S.T.; Caruso, R.A.; Doherty, C.M. Metal–organic frameworks for chemical sensing devices. *Mater. Horizons* **2021**, *8*, 2387–2419. [[CrossRef](#)] [[PubMed](#)]
44. Han, Z.; Wang, K.; Min, H.; Xu, J.; Shi, W.; Cheng, P. Bifunctionalized Metal–Organic Frameworks for Pore-Size-Dependent Enantioselective Sensing. *Angew. Chem. Int. Edit.* **2022**, *61*, e202204066. [[CrossRef](#)] [[PubMed](#)]
45. Younis, S.A.; Bhardwaj, N.; Bhardwaj, S.K.; Kim, K.-H.; Deep, A. Rare earth metal–organic frameworks (RE-MOFs): Synthesis, properties, and biomedical applications. *Coordin. Chem. Rev.* **2021**, *429*, 213620. [[CrossRef](#)]
46. Giliopoulos, D.; Zamboulis, A.; Giannakoudakis, D.; Bikiaris, D.; Triantafyllidis, K. Polymer/Metal Organic Framework (MOF) Nanocomposites for Biomedical Applications. *Molecules* **2020**, *25*, 185. [[CrossRef](#)]
47. Cun, J.-E.; Fan, X.; Pan, Q.; Gao, W.; Luo, K.; He, B.; Pu, Y. Copper-based metal–organic frameworks for biomedical applications. *Adv. Colloid Interface Sci.* **2022**, *305*, 102686. [[CrossRef](#)]
48. Fan, W.; Zhang, X.; Kang, Z.; Liu, X.; Sun, D. Isoreticular chemistry within metal–organic frameworks for gas storage and separation. *Coord. Chem. Rev.* **2021**, *443*, 213968. [[CrossRef](#)]
49. Amooaghin, A.E.; Sanaeepur, H.; Luque, R.; Garcia, H.; Chen, B. Fluorinated metal–organic frameworks for gas separation. *Chem. Soc. Rev.* **2022**, *51*, 7427–7508. [[CrossRef](#)]
50. Shi, Y.; Liang, B.; Lin, R.-B.; Zhang, C.; Chen, B. Gas Separation via Hybrid Metal–Organic Framework/Polymer Membranes. *Trends Chem.* **2020**, *2*, 254–269. [[CrossRef](#)]
51. Li, Y.; Wang, Y.; Fan, W.; Sun, D. Flexible metal–organic frameworks for gas storage and separation. *Dalton Trans.* **2022**, *51*, 4608–4618. [[CrossRef](#)] [[PubMed](#)]
52. Chen, Z.; Mian, M.R.; Lee, S.-J.; Chen, H.; Zhang, X.; Kirlikovali, K.O.; Shulda, S.; Melix, P.; Rosen, A.S.; Parilla, P.A.; et al. Fine-Tuning a Robust Metal–Organic Framework toward Enhanced Clean Energy Gas Storage. *J. Am. Chem. Soc.* **2021**, *143*, 18838–18843. [[CrossRef](#)] [[PubMed](#)]
53. Jones, N.B.; Gibbons, B.; Morris, A.J.; Morris, J.R.; Troya, D. Reversible Dissociation for Effective Storage of Diborane Gas within the UiO-66-NH₂ Metal–Organic Framework. *ACS Appl. Mater. Interfaces* **2022**, *14*, 8322–8332. [[CrossRef](#)] [[PubMed](#)]
54. Kim, T.; Lee, J.H.; Lee, G.; Lee, J.; Song, H.; Jho, J.Y.; Lee, H.H.; Kim, Y.H. Synthesis of a Carbonaceous Two-Dimensional Material. *ACS Appl. Mater. Interfaces* **2019**, *11*, 21308–21313. [[CrossRef](#)] [[PubMed](#)]
55. Sangwan, V.K.; Hersam, M.C. Electronic Transport in Two-Dimensional Materials. *Annu. Rev. Phys. Chem.* **2018**, *69*, 299–325. [[CrossRef](#)] [[PubMed](#)]
56. Ye, M.; Seo, H.; Galli, G. Spin coherence in two-dimensional materials. *NPJ Comput. Mater.* **2019**, *5*, 44. [[CrossRef](#)]
57. Liu, X.; Sachan, A.K.; Howell, S.T.; Conde-Rubio, A.; Knoll, A.W.; Boero, G.; Zenobi, R.; Brugger, J. Thermomechanical Nanostraining of Two-Dimensional Materials. *Nano Lett.* **2020**, *20*, 8250–8257. [[CrossRef](#)]
58. Sohler, T.D.P.; Gibertini, M.; Campi, D.; Pizzi, G.; Marzari, N. Valley-Engineering Mobilities in Two-Dimensional Materials. *Nano Lett.* **2019**, *19*, 3723–3729. [[CrossRef](#)]
59. Cheng, Y.; Wu, X.; Zhang, Z.; Sun, Y.; Zhao, Y.; Zhang, Y.; Zhang, G. Thermo-mechanical correlation in two-dimensional materials. *Nanoscale* **2021**, *13*, 1425–1442. [[CrossRef](#)]
60. Zhang, Y.; Mei, J.; Yan, C.; Liao, T.; Bell, J.; Sun, Z. Bioinspired 2D Nanomaterials: Bioinspired 2D Nanomaterials for Sustainable Applications (*Adv. Mater.* 18/2020). *Adv. Mater.* **2020**, *32*, 2070144. [[CrossRef](#)]
61. Szunerits, S. 2D nanomaterials for electroanalysis. *Anal. Bioanal. Chem.* **2021**, *413*, 661–662. [[CrossRef](#)] [[PubMed](#)]
62. Murali, A.; Lokhande, G.; Deo, K.A.; Brokesh, A.; Gaharwar, A.K. Emerging 2D nanomaterials for biomedical applications. *Mater. Today* **2021**, *50*, 276–302. [[CrossRef](#)] [[PubMed](#)]
63. Hasan, A.M.; Wang, Y.; Bowen, C.R.; Yang, Y. 2D Nanomaterials for Effective Energy Scavenging. *Nano-Micro Lett.* **2021**, *13*, 82. [[CrossRef](#)]
64. Huang, T.; Jiang, Y.; Shen, G.; Chen, D. Recent Advances of Two-Dimensional Nanomaterials for Electrochemical Capacitors. *ChemSuschem* **2020**, *13*, 1093–1113. [[CrossRef](#)] [[PubMed](#)]
65. He, X.; Zhu, Y.; Ma, B.; Xu, X.; Huang, R.; Cheng, L.; Zhu, R. Bioactive 2D nanomaterials for neural repair and regeneration. *Adv. Drug Deliv. Rev.* **2022**, *187*, 114379. [[CrossRef](#)] [[PubMed](#)]
66. Pimpilova, M.; Ivanova-Kolcheva, V.; Stoyanova, M.; Dimcheva, N. 2D Nanomaterial—Based Electrocatalyst for Water Soluble Hydroperoxide Reduction. *Catalysts* **2022**, *12*, 807. [[CrossRef](#)]
67. Shi, L.-N.; Cui, L.-T.; Ji, Y.-R.; Xie, Y.; Zhu, Y.-R.; Yi, T.-F. Towards high-performance electrocatalysts: Activity optimization strategy of 2D MXenes-based nanomaterials for water-splitting. *Coord. Chem. Rev.* **2022**, *469*, 214668. [[CrossRef](#)]
68. Li, Z.; Chen, Y.; Ma, T.; Jiang, Y.; Chen, J.; Pan, H.; Sun, W. 2D Metal-Free Nanomaterials Beyond Graphene and Its Analogues toward Electrocatalysis Applications. *Adv. Energy Mater.* **2021**, *11*, 2101202. [[CrossRef](#)]
69. Zheng, F.; Zhang, W.; Zhang, X.; Zhang, Y.; Chen, W. Sub-2 nm Ultrathin and Robust 2D FeNi Layered Double Hydroxide Nanosheets Packed with 1D FeNi-MOFs for Enhanced Oxygen Evolution Electrocatalysis. *Adv. Funct. Mater.* **2021**, *31*, 2103318. [[CrossRef](#)]
70. Pang, Y.; Su, C.; Jia, G.; Xu, L.; Shao, Z. Emerging two-dimensional nanomaterials for electrochemical nitrogen reduction. *Chem. Soc. Rev.* **2021**, *50*, 12744–12787. [[CrossRef](#)]

71. Zhao, G.; Liu, W.; Yuan, F.; Liu, J. Two host-guest 2D MOFs based on hexyl viologen cations: Photochromism. *Dye. Pigment.* **2021**, *188*, 109196. [[CrossRef](#)]
72. Chang, H.; Zhou, Y.; Zheng, X.; Liu, W.; Xu, Q. Single-Layer 2D Ni–BDC MOF Obtained in Supercritical CO₂-Assisted Aqueous Solution. *Chem.-Eur. J.* **2022**, *28*, e202201811. [[CrossRef](#)] [[PubMed](#)]
73. Choi, J.Y.; Flood, J.; Stodolka, M.; Pham, H.T.B.; Park, J. From 2D to 3D: Postsynthetic Pillar Insertion in Electrically Conductive MOF. *ACS Nano* **2022**, *16*, 3145–3151. [[CrossRef](#)] [[PubMed](#)]
74. Wang, L.; Saji, S.E.; Wu, L.; Wang, Z.; Chen, Z.; Du, Y.; Yu, X.; Zhao, H.; Yin, Z. Emerging Synthesis Strategies of 2D MOFs for Electrical Devices and Integrated Circuits. *Small* **2022**, *18*, e2201642. [[CrossRef](#)]
75. Dong, R.; Feng, X. Making large single crystals of 2D MOFs. *Nat. Mater.* **2021**, *20*, 122–123. [[CrossRef](#)]
76. Wei, H.; Tian, Y.; Chen, Q.; Estevez, D.; Xu, P.; Peng, H.-X.; Qin, F. Microwave absorption performance of 2D Iron-Quinoid MOF. *Chem. Eng. J.* **2021**, *405*, 126637. [[CrossRef](#)]
77. Majidi, L.; Ahmadiparidari, A.; Shan, N.; Misal, S.N.; Kumar, K.; Huang, Z.; Rastegar, S.; Hemmat, Z.; Zou, X.; Zapol, P.; et al. 2D Copper Tetrahydroxyquinone Conductive Metal–Organic Framework for Selective CO₂ Electrocatalysis at Low Overpotentials. *Adv. Mater.* **2021**, *33*, e2004393. [[CrossRef](#)]
78. Yang, D.; Zuo, S.; Yang, H.; Zhou, Y.; Lu, Q.; Wang, X. Tailoring Layer Number of 2D Porphyrin-Based MOFs Towards Photocoupled Electroreduction of CO₂. *Adv. Mater.* **2022**, *34*, e2107293. [[CrossRef](#)]
79. Tang, D.; Yang, X.; Wang, B.; Ding, Y.; Xu, S.; Liu, J.; Peng, Y.; Yu, X.; Su, Z.; Qin, X. One-Step Electrochemical Growth of 2D/3D Zn(II)-MOF Hybrid Nanocomposites on an Electrode and Utilization of a PtNPs@2D MOF Nanocatalyst for Electrochemical Immunoassay. *ACS Appl. Mater. Interfaces* **2021**, *13*, 46225–46232. [[CrossRef](#)]
80. Lee, M.K.; Shokouhimehr, M.; Kim, S.Y.; Jang, H.W. Two-Dimensional Metal–Organic Frameworks and Covalent–Organic Frameworks for Electrocatalysis: Distinct Merits by the Reduced Dimension. *Adv. Energy Mater.* **2021**, *12*, 2003990. [[CrossRef](#)]
81. Meng, R.; Du, Q.; Zhong, N.; Zhou, X.; Liu, S.; Yin, S.; Liang, X. A Tandem Electrocatalysis of Sulfur Reduction by Bimetal 2D MOFs. *Adv. Energy Mater.* **2021**, *11*, 2102819. [[CrossRef](#)]
82. Wang, H.-Y.; Sun, X.-B.; Wang, G.-S. A MXene-modulated 3D crosslinking network of hierarchical flower-like MOF derivatives towards ultra-efficient microwave absorption properties. *J. Mater. Chem. A* **2021**, *9*, 24571–24581. [[CrossRef](#)]
83. Song, Y.; Song, X.; Wang, X.; Bai, J.; Cheng, F.; Lin, C.; Wang, X.; Zhang, H.; Sun, J.; Zhao, T.; et al. Two-Dimensional Metal–Organic Framework Superstructures from Ice-Templated Self-Assembly. *J. Am. Chem. Soc.* **2022**, *144*, 17457–17467. [[CrossRef](#)] [[PubMed](#)]
84. Zhang, W.-D.; Zhou, L.; Wang, H.-R.; Xu, H.; Zhu, H.; Jiang, Y.; Yan, X.; Gu, Z.-G. A Hexagonal Nut-Like Metal–Organic Framework and Its Conformal Transformation. *Small* **2022**, *18*, 2203356. [[CrossRef](#)]
85. Wei, Y.; Zou, L.; Wang, H.; Wang, Y.; Xu, Q. Micro/Nano-Scaled Metal–Organic Frameworks and Their Derivatives for Energy Applications. *Adv. Energy Mater.* **2022**, *12*, 2003970. [[CrossRef](#)]
86. Huang, K.; Guo, S.; Wang, R.; Lin, S.; Hussain, N.; Wei, H.; Deng, B.; Long, Y.; Lei, M.; Tang, H.; et al. Two-dimensional MOF/MOF derivative arrays on nickel foam as efficient bifunctional coupled oxygen electrodes. *Chin. J. Catal.* **2020**, *41*, 1754–1760. [[CrossRef](#)]
87. Gao, Z.; Ma, H.; Yuan, S.; Ren, H.; Ge, Z.; Zhu, H.; Guo, W.; Ding, F.; Zhao, W. Benzenehexol-based 2D MOF as high-performance electrocatalyst for oxygen reduction reaction. *Appl. Surf. Sci.* **2022**, *601*, 154187. [[CrossRef](#)]
88. Huo, M.; Sun, T.; Wang, Y.; Sun, P.; Dang, J.; Wang, B.; Dharanipragada, N.V.R.A.; Inge, A.K.; Zhang, W.; Cao, R.; et al. A heteroepitaxially grown two-dimensional metal–organic framework and its derivative for the electrocatalytic oxygen reduction reaction. *J. Mater. Chem. A* **2022**, *10*, 10408–10416. [[CrossRef](#)]
89. Pang, W.; Shao, B.; Tan, X.-Q.; Tang, C.; Zhang, Z.; Huang, J. Exfoliation of metal–organic frameworks into efficient single-layer metal–organic nanosheet electrocatalysts by the synergistic action of host–guest interactions and sonication. *Nanoscale* **2020**, *12*, 3623–3629. [[CrossRef](#)]
90. Villalpando, G.; Ferrenti, A.M.; Singha, R.; Song, X.; Cheng, G.; Yao, N.; Schoop, L.M. Chemical Exfoliation toward Magnetic 2D VOCl Monolayers. *ACS Nano* **2022**, *16*, 13814–13820. [[CrossRef](#)]
91. Wang, F.; Liu, Z.; Cheng, Z. Ultrasonic-assisted exfoliation for 2D Zn(Bim)(OAc) nanosheets used as an oil-soluble additive in lubricants. *Appl. Organomet. Chem.* **2020**, *34*, e5950. [[CrossRef](#)]
92. Nicks, J.; Foster, J.A. Post-exfoliation functionalisation of metal–organic framework nanosheets via click chemistry. *Nanoscale* **2022**, *14*, 6220–6227. [[CrossRef](#)]
93. Nian, P.; Liu, H.; Zhang, X. Bottom-up synthesis of 2D Co-based metal–organic framework nanosheets by an ammonia-assisted strategy for tuning the crystal morphology. *CrystEngComm* **2019**, *21*, 3199–3208. [[CrossRef](#)]
94. Jia, J.; Wei, L.; Li, F.; Yu, C.; Yang, K.; Liang, T. In situ growth of NiFe MOF/NF by controlling solvent mixtures as efficient electrocatalyst in oxygen evolution. *Inorg. Chem. Commun.* **2021**, *128*, 108605. [[CrossRef](#)]
95. Song, D.; Guo, H.; Huang, K.; Zhang, H.; Chen, J.; Wang, L.; Lian, C.; Wang, Y. Carboxylated carbon quantum dot-induced binary metal–organic framework nanosheet synthesis to boost the electrocatalytic performance. *Mater. Today* **2022**, *54*, 42–51. [[CrossRef](#)]
96. Zeng, R.; He, T.; Lu, L.; Li, K.; Luo, Z.; Cai, K. Ultra-thin metal–organic framework nanosheets for chemo-photodynamic synergistic therapy. *J. Mater. Chem. B* **2021**, *9*, 4143–4153. [[CrossRef](#)]
97. Zhang, H.; Li, Q.; Weng, B.; Xiao, L.; Tian, Z.; Yang, J.; Liu, T.; Lai, F. Edge engineering of platinum nanoparticles via porphyrin-based ultrathin 2D metal–organic frameworks for enhanced photocatalytic hydrogen generation. *Chem. Eng. J.* **2022**, *442*, 136144. [[CrossRef](#)]
98. Yaghi, O.M. Evolution of MOF single crystals. *Chem* **2022**, *8*, 1541–1543. [[CrossRef](#)]

99. Suresh, K.; Aulakh, D.; Purewal, J.; Siegel, D.J.; Veenstra, M.; Matzger, A.J. Optimizing Hydrogen Storage in MOFs through Engineering of Crystal Morphology and Control of Crystal Size. *J. Am. Chem. Soc.* **2021**, *143*, 10727–10734. [[CrossRef](#)]
100. Li, Q.; Wang, Q.; Li, Y.; Zhang, X.; Huang, Y. 2D bimetallic Ni/Fe MOF nanosheet composites as a peroxidase-like nanozyme for colorimetric assay of multiple targets. *Anal. Methods* **2021**, *13*, 2066–2074. [[CrossRef](#)]
101. Luo, Y.-H.; Ma, S.-H.; Dong, H.; Zou, Y.-C.; Xu, K.-X.; Su, S.; Jin, X.-W.; Zhang, L.; Fang, W.-X. Two-dimensional nanosheets of metal–organic frameworks with tailorable morphologies. *Mater. Today Chem.* **2021**, *22*, 100517. [[CrossRef](#)]
102. Wang, X.; Zhang, H.; Yang, Z.; Zhang, C.; Liu, S. Ultrasound-treated metal-organic framework with efficient electrocatalytic oxygen evolution activity. *Ultrason. Sonochem.* **2019**, *59*, 104714. [[CrossRef](#)] [[PubMed](#)]
103. Amo-Ochoa, P.; Welte, L.; González-Prieto, R.; Miguel, P.J.S.; Gómez-García, C.J.; Mateo-Martí, E.; Delgado, S.; Gómez-Herrero, J.; Zamora, F. Single layers of a multifunctional laminar Cu(I,II) coordination polymer. *Chem. Commun.* **2010**, *46*, 3262–3264. [[CrossRef](#)] [[PubMed](#)]
104. Tamuly, P.; Sama, F.; Moorthy, J.N. Metal–Organic Nanosheets (MONs): Exfoliation by Mechanical Grinding and Iodine Capture. *Adv. Mater. Interfaces* **2022**, *9*, 2200337. [[CrossRef](#)]
105. Wang, M.; Shi, H.; Zhang, P.; Liao, Z.; Wang, M.; Zhong, H.; Schwotzer, F.; Nia, A.S.; Zschech, E.; Zhou, S.; et al. Phthalocyanine-Based 2D Conjugated Metal–Organic Framework Nanosheets for High-Performance Micro-Supercapacitors. *Adv. Funct. Mater.* **2020**, *30*, 2002664. [[CrossRef](#)]
106. Han, L.-J.; Zheng, D.; Chen, S.-G.; Zheng, H.-G.; Ma, J. A Highly Solvent-Stable Metal–Organic Framework Nanosheet: Morphology Control, Exfoliation, and Luminescent Property. *Small* **2018**, *14*, 1703873. [[CrossRef](#)]
107. Shen, Y.; Shan, B.; Cai, H.; Qin, Y.; Agarwal, A.; Trivedi, D.B.; Chen, B.; Liu, L.; Zhuang, H.; Mu, B.; et al. Ultimate Control over Hydrogen Bond Formation and Reaction Rates for Scalable Synthesis of Highly Crystalline vdW MOF Nanosheets with Large Aspect Ratio. *Adv. Mater.* **2018**, *30*, e1802497. [[CrossRef](#)]
108. Peng, Y.; Li, Y.; Ban, Y.; Yang, W. Two-Dimensional Metal–Organic Framework Nanosheets for Membrane-Based Gas Separation. *Angew. Chem. Int. Edit.* **2017**, *56*, 9757–9761. [[CrossRef](#)]
109. Ding, Y.; Chen, Y.-P.; Zhang, X.; Chen, L.; Dong, Z.; Jiang, H.-L.; Xu, H.; Zhou, H.-C. Controlled Intercalation and Chemical Exfoliation of Layered Metal–Organic Frameworks Using a Chemically Labile Intercalating Agent. *J. Am. Chem. Soc.* **2017**, *139*, 9136–9139. [[CrossRef](#)]
110. Qin, M.-F.; Mu, Q.-Q.; Bao, S.-S.; Liang, X.; Peng, Y.; Zheng, L.-M. Chemically Exfoliated Semiconducting Bimetallic Porphyrinylphosphonate Metal–Organic Layers for Photocatalytic CO₂ Reduction under Visible Light. *ACS Appl. Energy Mater.* **2021**, *4*, 4319–4326. [[CrossRef](#)]
111. Huang, J.; Li, Y.; Huang, R.; He, C.; Gong, L.; Hu, Q.; Wang, L.; Xu, Y.; Tian, X.; Liu, S.; et al. Electrochemical Exfoliation of Pillared-Layer Metal–Organic Framework to Boost the Oxygen Evolution Reaction. *Angew. Chem. Int. Ed.* **2018**, *57*, 4632–4636. [[CrossRef](#)]
112. Li, H.; Hou, J.; Bennett, T.D.; Liu, J.; Zhang, Y. Templated growth of vertically aligned 2D metal–organic framework nanosheets. *J. Mater. Chem. A* **2019**, *7*, 5811–5818. [[CrossRef](#)]
113. Wang, S.; Wang, T.; Zheng, H.; Fan, F.; Gu, Z.; He, W.; Zhang, B.; Shao, L.; Chen, H.; Li, Y.; et al. Fabrication of mesoporous MOF nanosheets via surfactant-template method for C–S coupling reactions. *Microporous Mesoporous Mater.* **2020**, *303*, 110254. [[CrossRef](#)]
114. Han, M.; Zhang, X.; Gao, H.; Chen, S.; Cheng, P.; Wang, P.; Zhao, Z.; Dang, R.; Wang, G. In situ semi-sacrificial template-assisted growth of ultrathin metal–organic framework nanosheets for electrocatalytic oxygen evolution. *Chem. Eng. J.* **2021**, *426*, 131348. [[CrossRef](#)]
115. Chen, I.-F.; Lu, C.-F.; Su, W.-F. Highly Conductive 2D Metal–Organic Framework Thin Film Fabricated by Liquid–Liquid Interfacial Reaction Using One-Pot-Synthesized Benzenehexathiol. *Langmuir* **2018**, *34*, 15754–15762. [[CrossRef](#)]
116. Wang, M.; Dong, X.; Meng, Z.; Hu, Z.; Lin, Y.; Peng, C.; Wang, H.; Pao, C.; Ding, S.; Li, Y.; et al. An Efficient Interfacial Synthesis of Two-Dimensional Metal–Organic Framework Nanosheets for Electrochemical Hydrogen Peroxide Production. *Angew. Chem. Int. Ed.* **2021**, *60*, 11190–11195. [[CrossRef](#)]
117. Rodenas, T.; Luz, I.; Prieto, G.; Seoane, B.; Miro, H.; Corma, A.; Kapteijn, F.; Llabrés, I.; Xamena, F.X.; Gascon, J. Metal–organic framework nanosheets in polymer composite materials for gas separation. *Nat. Mater.* **2014**, *14*, 48–55. [[CrossRef](#)]
118. Zhao, M.; Wang, Y.; Ma, Q.; Huang, Y.; Zhang, X.; Ping, J.; Zhang, Z.; Lu, Q.; Yu, Y.; Xu, H.; et al. Ultrathin 2D Metal–Organic Framework Nanosheets. *Adv. Mater.* **2015**, *27*, 7372–7378. [[CrossRef](#)]
119. Ma, J.; Bai, W.; Liu, X.; Zheng, J. Electrochemical dopamine sensor based on bi-metallic Co/Zn porphyrin metal–organic framework. *Microchim. Acta* **2021**, *189*, 20. [[CrossRef](#)]
120. Abdelhamid, H.N. Surfactant assisted synthesis of hierarchical porous metal-organic frameworks nanosheets. *Nanotechnology* **2019**, *30*, 435601. [[CrossRef](#)]
121. Fan, H.; Yu, H.; Wu, X.; Zhang, Y.; Luo, Z.; Wang, H.; Guo, Y.; Madhavi, S.; Yan, Q. Controllable Preparation of Square Nickel Chalcogenide (NiS and NiSe₂) Nanoplates for Superior Li/Na Ion Storage Properties. *ACS Appl. Mater. Interfaces* **2016**, *8*, 25261–25267. [[CrossRef](#)] [[PubMed](#)]
122. Zhang, X.; Zhang, P.; Chen, C.; Zhang, J.; Yang, G.; Zheng, L.; Zhang, J.; Han, B. Fabrication of 2D metal–organic framework nanosheets with tailorable thickness using bio-based surfactants and their application in catalysis. *Green Chem.* **2019**, *21*, 54–58. [[CrossRef](#)]

123. Lin, Y.; Wan, H.; Wu, D.; Chen, G.; Zhang, N.; Liu, X.; Li, J.; Cao, Y.; Qiu, G.; Ma, R. Metal-Organic Framework Hexagonal Nanoplates: Bottom-up Synthesis, Topotactic Transformation, and Efficient Oxygen Evolution Reaction. *J. Am. Chem. Soc.* **2020**, *142*, 7317–7321. [[CrossRef](#)] [[PubMed](#)]
124. Lin, Y.; Chen, G.; Wan, H.; Chen, F.; Liu, X.; Ma, R. 2D Free-Standing Nitrogen-Doped Ni-Ni₃S₂@Carbon Nanoplates Derived from Metal–Organic Frameworks for Enhanced Oxygen Evolution Reaction. *Small* **2019**, *15*, 1900348. [[CrossRef](#)] [[PubMed](#)]
125. He, S.; Chen, Y.; Zhang, Z.; Ni, B.; He, W.; Wang, X. Competitive coordination strategy for the synthesis of hierarchical-pore metal–organic framework nanostructures. *Chem. Sci.* **2016**, *7*, 7101–7105. [[CrossRef](#)]
126. Cliffe, M.J.; Castillo-Martínez, E.; Wu, Y.; Lee, J.; Forse, A.C.; Firth, F.C.N.; Moghadam, P.Z.; Fairen-Jimenez, D.; Gaultois, M.W.; Hill, J.A.; et al. Metal–Organic Nanosheets Formed via Defect-Mediated Transformation of a Hafnium Metal–Organic Framework. *J. Am. Chem. Soc.* **2017**, *139*, 5397–5404. [[CrossRef](#)]
127. Zheng, G.; Xing, Z.; Gao, X.; Nie, C.; Xu, Z.; Ju, Z. Fabrication of 2D Cu-BDC MOF and its derived porous carbon as anode material for high-performance Li/K-ion batteries. *Appl. Surf. Sci.* **2021**, *559*, 149701. [[CrossRef](#)]
128. Zhao, X.; Xu, H.; Hui, Z.; Sun, Y.; Yu, C.; Xue, J.; Zhou, R.; Wang, L.; Dai, H.; Zhao, Y.; et al. Electrostatically Assembling 2D Nanosheets of MXene and MOF-Derivatives into 3D Hollow Frameworks for Enhanced Lithium Storage. *Small* **2019**, *15*, e1904255. [[CrossRef](#)]
129. Wang, Q.; Yang, R.; Li, J.; Yang, Y.; Wu, Y.; Zhou, X.; Ma, G.; Ren, S. 2D DUT-8(Ni)-derived Ni@C nanosheets for efficient hydrogen evolution. *J. Solid State Electrochem.* **2020**, *24*, 2461–2467. [[CrossRef](#)]
130. Ren, J.-T.; Zheng, Y.-L.; Yuan, K.; Zhou, L.; Wu, K.; Zhang, Y.-W. Self-templated synthesis of Co₃O₄ hierarchical nanosheets from a metal–organic framework for efficient visible-light photocatalytic CO₂ reduction. *Nanoscale* **2020**, *12*, 755–762. [[CrossRef](#)]
131. He, P.; Xie, Y.; Dou, Y.; Zhou, J.; Zhou, A.; Wei, X.; Li, J.-R. Partial Sulfurization of a 2D MOF Array for Highly Efficient Oxygen Evolution Reaction. *ACS Appl. Mater. Interfaces* **2019**, *11*, 41595–41601. [[CrossRef](#)] [[PubMed](#)]
132. Contreras-Pereda, N.; Moghzi, F.; Baselga, J.; Zhong, H.; Janczak, J.; Soleimannejad, J.; Dong, R.; Ruiz-Molina, D. Ultrasound-assisted exfoliation of a layered 2D coordination polymer with HER electrocatalytic activity. *Ultrason. Sonochem.* **2021**, *70*, 105292. [[CrossRef](#)] [[PubMed](#)]
133. Cheng, J.; Yang, X.; Yang, X.; Xia, R.; Xu, Y.; Sun, W.; Zhou, J. Hierarchical Ni₃S₂@2D Co MOF nanosheets as efficient hetero-electrocatalyst for hydrogen evolution reaction in alkaline solution. *Fuel Process. Technol.* **2022**, *229*, 107174. [[CrossRef](#)]
134. Zhou, Y.; Chen, Y.; Wei, M.; Fan, H.; Liu, X.; Liu, Q.; Liu, Y.; Cao, J.; Yang, L. 2D MOF-derived porous NiCoSe nanosheet arrays on Ni foam for overall water splitting. *CrystEngComm* **2021**, *23*, 69–81. [[CrossRef](#)]
135. Wang, Z.; Zhang, X.; Rezazadeh, A. Hydrogen fuel and electricity generation from a new hybrid energy system based on wind and solar energies and alkaline fuel cell. *Energy Rep.* **2021**, *7*, 2594–2604. [[CrossRef](#)]
136. Li, W.; Wang, Y.; Xu, L.; Tang, Y.; Wu, X.; Liu, J. Thermodynamic evaluation of electricity and hydrogen cogeneration from solar energy and fossil fuels. *Energy Convers. Manag.* **2022**, *256*, 115344. [[CrossRef](#)]
137. Sekar, S.; Devi, S.B.; Maruthasalamoorthy, S.; Maiyalagan, T.; Kim, D.Y.; Lee, S.; Navamathavan, R. One-step facile hydrothermal synthesis of rGO-CoS₂ nanocomposites for high performance HER electrocatalysts. *Int. J. Hydrogen Energy* **2022**, *47*, 40359–40367. [[CrossRef](#)]
138. Habib, A.; Mandavkar, R.; Burse, S.; Lin, S.; Kulkarni, R.; Patil, C.S.; Jeong, J.-H.; Lee, J. Design of boron-based ternary W₃CoB₃ electrocatalyst for the improved HER and OER performances. *Mater. Today Energy* **2022**, *26*, 101021. [[CrossRef](#)]
139. Liang, T.; Xie, J.; Wang, A.; Ma, D.; Mao, Z.; Wang, J.; Li, H. Prediction of HER electrocatalyst with enhanced performance based on atoms-doped black phosphorene: A first-principles study. *Appl. Surf. Sci.* **2022**, *604*, 154508. [[CrossRef](#)]
140. Prats, H.; Chan, K. The determination of the HOR/HER reaction mechanism from experimental kinetic data. *Phys. Chem. Chem. Phys.* **2021**, *23*, 27150–27158. [[CrossRef](#)]
141. Ma, R.; Hong, K. Theoretical Investigation of HER Mechanism Using Density Functional and Ab Initio Calculations. *Bull. Korean Chem. Soc.* **2021**, *42*, 1289–1292. [[CrossRef](#)]
142. Lin, S.; Zhang, T.; Zhang, J.; Li, Y. The Mechanism of One-Step Synthesis of Oxides from Metal Chlorides and Their Electrocatalytic HER Study. *Cryst. Res. Technol.* **2022**, *57*, 2200008. [[CrossRef](#)]
143. Jin, Q.; Liu, N.; Dai, C.; Xu, R.; Wu, B.; Yu, G.; Chen, B.; Du, Y. H₂-Directing Strategy on In Situ Synthesis of Co-MoS₂ with Highly Expanded Interlayer for Elegant HER Activity and its Mechanism. *Adv. Energy Mater.* **2020**, *10*, 2000291. [[CrossRef](#)]
144. Zhang, C.; Yang, S.; Rao, D. Theoretical study the component and facet dependence of HER performance on nickel phosphides surfaces. *Int. J. Hydrogen Energy* **2022**, *47*, 2992–3000. [[CrossRef](#)]
145. Wu, T.; Melander, M.M.; Honkala, K. Coadsorption of NRR and HER Intermediates Determines the Performance of Ru-N₄ toward Electrocatalytic N₂ Reduction. *ACS Catal.* **2022**, *12*, 2505–2512. [[CrossRef](#)]
146. Karthick, K.; Basha, A.B.M.; Sivakumaran, A.; Kundu, S. Enhancement of HER kinetics with RhNiFe for high-rate water electrolysis. *Catal. Sci. Technol.* **2020**, *10*, 3681–3693. [[CrossRef](#)]
147. Zhu, J.; Tu, Y.; Cai, L.; Ma, H.; Chai, Y.; Zhang, L.; Zhang, W. Defect-Assisted Anchoring of Pt Single Atoms on MoS₂ Nanosheets Produces High-Performance Catalyst for Industrial Hydrogen Evolution Reaction. *Small* **2021**, *18*, 2104824. [[CrossRef](#)]
148. Yasin, G.; Ibraheem, S.; Ali, S.; Arif, M.; Ibrahim, S.; Iqbal, R.; Kumar, A.; Tabish, M.; Mushtaq, M.; Saad, A.; et al. Defects-engineered tailoring of tri-doped interlinked metal-free bifunctional catalyst with lower gibbs free energy of OER/HER intermediates for overall water splitting. *Mater. Today Chem.* **2022**, *23*, 100634. [[CrossRef](#)]

149. Ohm, D.; Domke, K.F. Controlled deposition of 2D-confined Pd or Ir nano-islands on Au(111) following Cu UPD, and their HER activity. *Electroanal. Chem.* **2021**, *896*, 115285. [[CrossRef](#)]
150. Zhang, C.; Liang, X.; Xu, R.; Dai, C.; Wu, B.; Yu, G.; Chen, B.; Wang, X.; Liu, N. H₂ In Situ Inducing Strategy on Pt Surface Segregation Over Low Pt Doped PtNi₅ Nanoalloy with Superhigh Alkaline HER Activity. *Adv. Funct. Mater.* **2021**, *31*, 2008298. [[CrossRef](#)]
151. Sun, C.; Duan, X.; Song, J.; Zhang, M.; Jin, Y.; Zhang, M.; Song, L.; Cao, H. Rh particles in N-doped porous carbon materials derived from ZIF-8 as an efficient bifunctional electrocatalyst for the ORR and HER. *RSC Adv.* **2021**, *11*, 13906–13911. [[CrossRef](#)] [[PubMed](#)]
152. Liu, C.; Pan, G.; Liang, N.; Hong, S.; Ma, J.; Liu, Y. Ir Single Atom Catalyst Loaded on Amorphous Carbon Materials with High HER Activity. *Adv. Sci.* **2022**, *9*, e2105392. [[CrossRef](#)]
153. Sarkar, S.; Peter, S.C. An overview on Pd-based electrocatalysts for the hydrogen evolution reaction. *Inorg. Chem. Front.* **2018**, *5*, 2060–2080. [[CrossRef](#)]
154. Liang, L.; Jin, H.; Zhou, H.; Liu, B.; Hu, C.; Chen, D.; Wang, Z.; Hu, Z.; Zhao, Y.; Li, H.-W.; et al. Cobalt single atom site isolated Pt nanoparticles for efficient ORR and HER in acid media. *Nano Energy* **2021**, *88*, 106221. [[CrossRef](#)]
155. Li, D.; Chen, X.; Lv, Y.; Zhang, G.; Huang, Y.; Liu, W.; Li, Y.; Chen, R.; Nuckolls, C.; Ni, H. An effective hybrid electrocatalyst for the alkaline HER: Highly dispersed Pt sites immobilized by a functionalized NiRu-hydroxide. *Appl. Catal. B-Environ.* **2020**, *269*, 118824. [[CrossRef](#)]
156. Chen, C.; Suo, N.; Han, X.; He, X.; Dou, Z.; Lin, Z.; Cui, L. Tuning the morphology and electron structure of metal-organic framework-74 as bifunctional electrocatalyst for OER and HER using bimetallic collaboration strategy. *J. Alloys Compd.* **2021**, *865*, 158795. [[CrossRef](#)]
157. Li, Q.; Zhou, Y.; Chen, C.; Liu, Q.; Huo, J.; Yi, H. Building CoP/Co-MOF heterostructure in 2D nanosheets for improving electrocatalytic hydrogen evolution over a wide pH range. *Electroanal. Chem.* **2021**, *895*, 115514. [[CrossRef](#)]
158. Chhetri, K.; Muthurasu, A.; Dahal, B.; Kim, T.; Mukhiya, T.; Chae, S.-H.; Ko, T.; Choi, Y.; Kim, H. Engineering the abundant heterointerfaces of integrated bimetallic sulfide-coupled 2D MOF-derived mesoporous CoS₂ nanoarray hybrids for electrocatalytic water splitting. *Mater. Today Nano* **2022**, *17*, 100146. [[CrossRef](#)]
159. Zeng, Y.; Cao, Z.; Liao, J.; Liang, H.; Wei, B.; Xu, X.; Xu, H.; Zheng, J.; Zhu, W.; Cavallo, L.; et al. Construction of hydroxide pn junction for water splitting electrocatalysis. *Appl. Catal. B Environ.* **2021**, *292*, 120160. [[CrossRef](#)]
160. Martinez, J.; Mazarío, J.; Olloqui-Sariego, J.L.; Calvente, J.J.; Darawsheh, M.D.; Mínguez-Espallargas, G.; Domine, M.E.; Oña-Burgos, P. Bimetallic Intersection in PdFe@FeOx-C Nanomaterial for Enhanced Water Splitting Electrocatalysis. *Adv. Sustain. Syst.* **2022**, *6*, 2200096. [[CrossRef](#)]
161. Wang, Z.; Wang, P.; Zhang, H.; Tian, W.; Xu, Y.; Li, X.; Wang, L.; Wang, H. Construction of hierarchical IrTe nanotubes with assembled nanosheets for overall water splitting electrocatalysis. *J. Mater. Chem. A* **2021**, *9*, 18576–18581. [[CrossRef](#)]
162. Ai, L.; Chen, M.; Wang, X.; Luo, Y.; Wei, W.; Jiang, J. Localized photothermal heating of phosphate-incorporated iron oxide nanosheets enables greatly enhanced water splitting electrocatalysis. *J. Alloys Compd.* **2022**, *925*, 166750. [[CrossRef](#)]
163. Zhu, W.; Chen, W.; Yu, H.; Zeng, Y.; Ming, F.; Liang, H.; Wang, Z. NiCo/NiCo–OH and NiFe/NiFe–OH core shell nanostructures for water splitting electrocatalysis at large currents. *Appl. Catal. B Environ.* **2020**, *278*, 119326. [[CrossRef](#)]
164. Wang, X.; Wang, J.; Liao, J.; Wang, L.; Li, M.; Xu, R.; Yang, L. Surface engineering of superhydrophilic Ni₂P@NiFe LDH heterostructure toward efficient water splitting electrocatalysis. *Appl. Surf. Sci.* **2022**, *602*, 154287. [[CrossRef](#)]
165. Zhu, Z.; Xu, K.; Guo, W.; Zhang, H.; Xiao, X.; He, M.; Yu, T.; Zhao, H.; Zhang, D.; Yang, T. Vanadium-phosphorus incorporation induced interfacial modification on cobalt catalyst and its super electrocatalysis for water splitting in alkaline media. *Appl. Catal. B Environ.* **2022**, *304*, 120985. [[CrossRef](#)]
166. Wang, Y.; Guo, W.; Zhu, Z.; Xu, K.; Zhang, H.; Wei, W.; Xiao, X.; Liang, W.; He, M.; Yu, T.; et al. Interfacial boron modification on mesoporous octahedral rhodium shell and its enhanced electrocatalysis for water splitting and oxygen reduction. *Chem. Eng. J.* **2022**, *435*, 134982. [[CrossRef](#)]
167. Liang, T.; Lenus, S.; Liu, Y.; Chen, Y.; Sakthivel, T.; Chen, F.; Ma, F.; Dai, Z. Interface and M³⁺/M²⁺ Valence Dual-Engineering on Nickel Cobalt Sulfoselenide/Black Phosphorus Heterostructure for Efficient Water Splitting Electrocatalysis. *Energy Environ. Mater.* **2021**, *6*, e12332.
168. Yi, L.; Feng, B.; Chen, N.; Li, W.; Li, J.; Fang, C.; Yao, Y.; Hu, W. Electronic interaction boosted electrocatalysis of iridium nanoparticles on nitrogen-doped graphene for efficient overall water splitting in acidic and alkaline media. *Chem. Eng. J.* **2021**, *415*, 129034. [[CrossRef](#)]
169. Huang, R.; Wen, Y.; Peng, H.; Zhang, B. Improved kinetics of OER on Ru-Pb binary electrocatalyst by decoupling proton-electron transfer. *Chin. J. Catal.* **2022**, *43*, 130–138. [[CrossRef](#)]
170. Binninger, T.; Doublet, M.-L. The Ir–OOO–Ir transition state and the mechanism of the oxygen evolution reaction on IrO₂(110). *Energy Environ. Sci.* **2022**, *15*, 2519–2528. [[CrossRef](#)]
171. Moysiadou, A.; Lee, S.; Hsu, C.-S.; Chen, H.M.; Hu, X. Mechanism of Oxygen Evolution Catalyzed by Cobalt Oxyhydroxide: Cobalt Superoxide Species as a Key Intermediate and Dioxygen Release as a Rate-Determining Step. *J. Am. Chem. Soc.* **2020**, *142*, 11901–11914. [[CrossRef](#)] [[PubMed](#)]
172. Liu, X.; Zhang, G.; Wang, L.; Fu, H. Structural Design Strategy and Active Site Regulation of High-Efficient Bifunctional Oxygen Reaction Electrocatalysts for Zn–Air Battery. *Small* **2021**, *17*, e2006766. [[CrossRef](#)] [[PubMed](#)]

173. Hai, G.; Gao, H.; Huang, X.; Tan, L.; Xue, X.; Feng, S.; Wang, G. An efficient factor for fast screening of high-performance two-dimensional metal–organic frameworks towards catalyzing the oxygen evolution reaction. *Chem. Sci.* **2022**, *13*, 4397–4405. [[CrossRef](#)] [[PubMed](#)]
174. Zhao, Z.-Y.; Sun, X.; Gu, H.; Niu, Z.; Braunstein, P.; Lang, J.-P. Engineering the Electronic Structures of Metal–Organic Framework Nanosheets via Synergistic Doping of Metal Ions and Counteranions for Efficient Water Oxidation. *ACS Appl. Mater. Interfaces* **2022**, *14*, 15133–15140. [[CrossRef](#)] [[PubMed](#)]
175. An, H.; Hu, Y.; Song, N.; Mu, T.; Bai, S.; Peng, Y.; Liu, L.-L.; Tang, Y. Two-dimensional heterostructures built from ultrathin CeO₂ nanosheet surface-coordinated and confined metal–organic frameworks with enhanced stability and catalytic performance. *Chem. Sci.* **2022**, *13*, 3035–3044. [[CrossRef](#)] [[PubMed](#)]
176. Wei, X.; Cao, S.; Xu, H.; Jiang, C.; Wang, Z.; Ouyang, Y.; Lu, X.; Dai, F.; Sun, D. Novel Two-Dimensional Metal Organic Frameworks: High-Performance Bifunctional Electrocatalysts for OER/ORR. *ACS Mater. Lett.* **2022**, *4*, 1991–1998. [[CrossRef](#)]
177. Wang, Y.; Zhang, J. Structural engineering of transition metal-based nanostructured electrocatalysts for efficient water splitting. *Front. Chem. Sci. Eng.* **2018**, *12*, 838–854. [[CrossRef](#)]
178. Liu, Q.; Chen, J.; Yang, P.; Yu, F.; Liu, Z.; Peng, B. Directly application of bimetallic 2D-MOF for advanced electrocatalytic oxygen evolution. *Int. J. Hydrogen Energy* **2021**, *46*, 416–424. [[CrossRef](#)]
179. Ge, K.; Sun, S.; Zhao, Y.; Yang, K.; Wang, S.; Zhang, Z.; Cao, J.; Yang, Y.; Zhang, Y.; Pan, M.; et al. Facile Synthesis of Two-Dimensional Iron/Cobalt Metal–Organic Framework for Efficient Oxygen Evolution Electrocatalysis. *Angew. Chem. Int. Ed.* **2021**, *60*, 12097–12102. [[CrossRef](#)]
180. Liu, Y.; Li, X.; Sun, Q.; Wang, Z.; Huang, W.; Guo, X.; Fan, Z.; Ye, R.; Zhu, Y.; Chueh, C.; et al. Freestanding 2D NiFe Metal–Organic Framework Nanosheets: Facilitating Proton Transfer via Organic Ligands for Efficient Oxygen Evolution Reaction. *Small* **2022**, *18*, e2201076. [[CrossRef](#)]
181. Park, K.; Kwon, J.; Jo, S.; Choi, S.; Enkhtuvshin, E.; Kim, C.; Lee, D.; Kim, J.; Sun, S.; Han, H.; et al. Simultaneous electrical and defect engineering of nickel iron metal-organic-framework via co-doping of metalloid and non-metal elements for a highly efficient oxygen evolution reaction. *Chem. Eng. J.* **2022**, *439*, 135720. [[CrossRef](#)]
182. Srinivas, K.; Lu, Y.; Chen, Y.; Zhang, W.; Yang, D. FeNi₃–Fe₃O₄ Heterogeneous Nanoparticles Anchored on 2D MOF Nanosheets/1D CNT Matrix as Highly Efficient Bifunctional Electrocatalysts for Water Splitting. *ACS Sustain. Chem. Eng.* **2020**, *8*, 3820–3831. [[CrossRef](#)]
183. Du, Y.-X.; Liu, L.; Li, Y.-K.; Liu, R.; Lu, W.-T.; Wang, J.-X.; Zhang, G.; Cao, F.-F. Fe-CoP/C composite nanoplate derived from 2D porphyrin MOF as an efficient catalyst for oxygen evolution reaction. *New J. Chem.* **2022**, *46*, 8271–8276. [[CrossRef](#)]
184. Li, S.; Wang, L.; Su, H.; Hong, A.N.; Wang, Y.; Yang, H.; Ge, L.; Song, W.; Liu, J.; Ma, T.; et al. Electron Redistributed S-Doped Nickel Iron Phosphides Derived from One-Step Phosphatization of MOFs for Significantly Boosting Electrochemical Water Splitting. *Adv. Funct. Mater.* **2022**, *32*, 2200733. [[CrossRef](#)]
185. Tian, J.; Xu, Y.; Li, J.; Chi, J.; Feng, L.; Pan, Q.; Li, X.; Su, Z. Post-decorated synthesis of metal-organic frameworks derived Ni/Ni₃S₂@CN electrocatalyst for efficient hydrogen evolution. *J. Solid State Chem.* **2022**, *313*, 123287. [[CrossRef](#)]
186. Li, S.; Wang, R.; Xie, M.; Xu, Y.; Chen, J.; Jiao, Y. Construction of trifunctional electrode material based on Pt-Coordinated Ce-Based metal organic framework. *J. Colloid Interface Sci.* **2022**, *622*, 378–389. [[CrossRef](#)]
187. Song, J.; Chen, J.-L.; Xu, Z.; Lin, R.Y.-Y. Metal–organic framework-derived 2D layered double hydroxide ultrathin nanosheets for efficient electrocatalytic hydrogen evolution reaction. *Chem. Commun.* **2022**, *58*, 10655–10658. [[CrossRef](#)]
188. Liu, P.; Li, J.; Yan, J.; Song, W. Defect-rich Fe-doped NiS/MoS₂ heterostructured ultrathin nanosheets for efficient overall water splitting. *Phys. Chem. Chem. Phys.* **2022**, *24*, 8344–8350. [[CrossRef](#)]
189. Wang, Y.; Wang, A.; Xue, Z.; Wang, L.; Li, X.; Wang, G. Ultrathin metal–organic framework nanosheet arrays and derived self-supported electrodes for overall water splitting. *J. Mater. Chem. A* **2021**, *9*, 22597–22602. [[CrossRef](#)]
190. Liu, H.; Huang, R.; Chen, W.; Zhang, Y.; Wang, M.; Hu, Y.; Zhou, Y.; Song, Y. Porous 2D cobalt–nickel phosphide triangular nanowall architecture assembled by 3D microsphere for enhanced overall water splitting. *Appl. Surf. Sci.* **2021**, *569*, 150762. [[CrossRef](#)]
191. Wang, Z.; Yu, K.; Huang, R.; Zhu, Z. Porous Co₃O₄ stabilized VS₂ nanosheets obtained with a MOF template for the efficient HER. *CrystEngComm* **2021**, *23*, 5097–5105. [[CrossRef](#)]
192. Ma, N.; Fei, C.; Wang, J.; Wang, Y. Fabrication of NiFe-MOF/cobalt carbonate hydroxide hydrate heterostructure for a high-performance electrocatalyst of oxygen evolution reaction. *J. Alloys Compd.* **2022**, *917*, 165511. [[CrossRef](#)]
193. Lin, Y.; Zhang, M.; Zhao, L.; Wang, L.; Cao, D.; Gong, Y. Ru doped bimetallic phosphide derived from 2D metal organic framework as active and robust electrocatalyst for water splitting. *Appl. Surf. Sci.* **2021**, *536*, 147952. [[CrossRef](#)]

Disclaimer/Publisher’s Note: The statements, opinions and data contained in all publications are solely those of the individual author(s) and contributor(s) and not of MDPI and/or the editor(s). MDPI and/or the editor(s) disclaim responsibility for any injury to people or property resulting from any ideas, methods, instructions or products referred to in the content.